Bioactive Materials 35 (2024) 99–121

Contents lists available at ScienceDirect

Bioactive Materials

journal homepage: www.keaipublishing.com/en/journals/bioactive-materials

A theragenerative bio-nanocomposite consisting of black phosphorus quantum dots for bone cancer therapy and regeneration

Ashkan Bigham [a,b], Ines Fasolino [a], Silvia Borsacchi [c,d], Carmen Valente [e], Lucia Calucci [c,d], Gabriele Turacchio [e,1], Marianna Pannico [f], Manuel Serrano-Ruiz [h], Luigi Ambrosio [a], Maria Grazia Raucci [a,*]

[a] Institute of Polymers, Composites and Biomaterials, National Research Council of Italy (IPCB-CNR), Viale John Fitzgerald Kennedy 54, Mostra d'Oltremare Padiglione 20, 80125, Naples, Italy
[b] Department of Chemical, Materials and Production Engineering, University of Naples Federico II, Piazzale V. Tecchio 80, 80125, Naples, Italy
[c] Institute for the Chemistry of OrganoMetallic Compounds-ICCOM, Italian National Research Council-CNR, via G. Moruzzi 1, 56124, Pisa, Italy
[d] Center for Instrument Sharing of the University of Pisa (CISUP), 56126, Pisa, Italy
[e] Institute of Experimental Endocrinology and Oncology "G. Salvatore" (IEOS), National Research Council (CNR), Via Pietro Castellino 111, 80131, Napoli, Italy
[f] Institute of Polymers, Composites, and Biomaterials, National Research Council of Italy (IPCB-CNR), Pozzuoli, Italy
[h] Institute for the Chemistry of OrganoMetallic Compounds-ICCOM, National Research Council-CNR, Sesto Fiorentino, Italy

ARTICLE INFO

Keywords:
Bioactive glass
Black phosphorus
Microwave treatment
Bone cancer therapy
Tissue regeneration

ABSTRACT

Recently, the term theragenerative has been proposed for biomaterials capable of inducing therapeutic approaches followed by repairing/regenerating the tissue/organ. This study is focused on the design of a new theragenerative nanocomposite composed of an amphiphilic non-ionic surfactant (Pluronic F127), bioactive glass (BG), and black phosphorus (BP). The nanocomposite was prepared through a two-step synthetic strategy, including a microwave treatment that turned BP nanosheets (BPNS) into quantum dots (BPQDs) with 5 ± 2 nm dimensions *in situ*. The effects of surfactant and microwave treatment were assessed *in vitro*: the surfactant distributes the ions homogenously throughout the composite and the microwave treatment chemically stabilizes the composite. The presence of BP enhanced bioactivity and promoted calcium phosphate formation in simulated body fluid. The inherent anticancer activity of BP-containing nanocomposites was tested against osteosarcoma cells *in vitro*, finding that 150 μg mL^{-1} was the lowest concentration which prevented the proliferation of SAOS-2 cells, while the counterpart without BP did not affect the cell growth rate. Moreover, the apoptosis pathways were evaluated and a mechanism of action was proposed. NIR irradiation was applied to induce further proliferation suppression on SAOS-2 cells through hyperthermia. The inhibitory effects of bare BP nanomaterials and nanocomposites on the migration and invasion of bone cancer, breast cancer, and prostate cancer cells were assessed *in vitro* to determine the anticancer potential of nanomaterials against primary and secondary bone cancers. The regenerative behavior of the nanocomposites was tested with healthy osteoblasts and human mesenchymal stem cells; the BPQDs-incorporated nanocomposite significantly promoted the proliferation of osteoblast cells and induced the osteogenic differentiation of stem cells. This study introduces a new multifunctional theragenerative platform with promising potential for simultaneous bone cancer therapy and regeneration.

1. Introduction

Progress in materials science has allowed the development of platforms beyond therapy. These platforms are composed of versatile biomaterials with different functionality and biological effects for biomedical applications [1]. For instance, theranostics come from therapy and diagnosis when combined into an agent. Having these two in one package allows early diagnosis and/or tracking of the treatment's

Peer review under responsibility of KeAi Communications Co., Ltd.
* Corresponding author.
E-mail address: mariagrazia.raucci@cnr.it (M.G. Raucci).
[1] Current address: Institute of Translational Pharmacology (IFT), National Research Council (CNR), Via Carducci 32, 67100, L'Aquila (Italy).

https://doi.org/10.1016/j.bioactmat.2024.01.018
Received 3 December 2023; Received in revised form 11 January 2024; Accepted 18 January 2024
Available online 24 January 2024

procedure. This is of particular interest in cancer therapy since obtaining accurate information in each step of treatment would give clues to direct the process towards cancer growth inhibition followed by suppression [2]. There is an up-and-coming term, theragenerative or therepair, which is the combination of therapy + regeneration and therapy + repair, respectively. Biomaterials endowed with these two features have attracted considerable attention in recent years specifically in wound healing and bone cancer therapy and regeneration [3,4]. Bone cancers are treated by first removing the tumor and then regenerating the defect. This is also the case for melanoma treatment which consists of the cancerous tissue resection in the first step and then wound regeneration [5,6]. Regarding the necessity of concurrent therapy and regeneration, the design of theragenerative packages is of great importance.

In the last decade, 2D materials in particular graphene and graphene oxide, have gained interest in biomedical applications due to extraordinary physicochemical properties including electrical conductivity, excellent mechanical properties, large surface area, easy-surface-functionalization, etc. [7]. Similar to graphene, but with thickness-dependent semiconducting properties, Mxenes like MoS_2 have also become very popular in cancer therapy. Although these materials have exhibited incredible potential in different biomedical applications, they show some shortcomings like lack of a bandgap in the case of graphene and low carrier mobility and cytotoxicity concerns in the case of Mxenes [8]. Discovered in 2014, exfoliated black phosphorus (BP) is a new 2D material that sparked considerable interest in different fields specifically in biomedical engineering. The distinctive properties of BP come from its structure in which each phosphorus atom with sp^3 hybridization makes a covalent bonding with three neighboring phosphorus atoms forming a layer arranged into a puckered honeycomb lattice that induces high anisotropy. This anisotropy endows BP with exceptional optical and electrical properties [9]. BP has a light absorption ranging from ultraviolet to near-infrared (NIR) and it can turn light into heat once exposed to irradiation. In the first biological window, depending on the wavelength, BP can induce heat (at around 808 nm) or the formation of reactive oxygen species (ROS) (606 nm) [10]. Photothermal- and photodynamic therapies are two therapeutic approaches widely applied in cancer therapy. The former relates to the generation of heat up to a degree that causes irreversible damage to cancerous cells without affecting the adjacent normal cells. The latter is based on the production of cytotoxic ROS as the result of being triggered with an external light source [11].

The advantages of 2D BP are as follows: it is an external stimuli-responsive agent with strong catalytic properties and its high surface area provides a suitable substrate for loading of biological moieties and drug molecules. Speaking of biocompatibility, once BP is oxidized and degraded, it turns into phosphate ions which are not cytotoxic and even can promote bone regeneration [12]. Above these benefits, BP stands out in 2D biomaterials because of its selective anticancer activity. In 2019, the inherent and selective chemotherapeutic effects of BP nanosheets (BPNSs) were reported. The nanosheets were tested against healthy and various cancer cell lines. Cancer cells promoted the biodegradation of nanosheets and the phosphate ions concentration was elevated due to intracellular oxidative stress and higher energy metabolism while no effect on the healthy cells was observed. It was found that G2/M phase arrest was obtained by the nanosheets leading to apoptosis and autophagy-related cancer cell death. Of note, BP revealed superior anticancer activity compared to doxorubicin, the well-known chemotherapeutic drug [13]. However, it remained unclear why the increase in the phosphate anions led to cancer cell death. In 2020, an update was reported on the possible mechanism of action of BPNSs towards cancer cells. HeLa, A549, H1299, and Hep3B were used as the cancer cell lines while D551 and Hek293 were adopted as the healthy cells. The results revealed that the nanosheets caused a decrease in the activity of dismutase by lipid peroxides culminating in higher ROS generation in cancer cells, whereas the ROS produced in the healthy cells was not too high to induce cytotoxicity [14]. Our research group has recently reported the selective anticancer potential of BP nanosheets towards osteosarcoma cells while promoting osteoblast cell proliferation. The nanosheets' efficacy was tested both in the presence and absence of NIR irradiation *in vitro*. The light irradiation was found to reinforce the anticancer activity of BP without negative effects behind the healthy ones [15]. Although BP has prominent pros, it is highly susceptible to oxidation in air and water leading to a significant decrease in its optical properties [16]. Therefore, considerable attention has been devoted to developing strategies to stabilize BP.

Different types of approaches have been tried to stabilize and/or protect BP from oxidation once used for biological applications. Surface modifications were applied mostly in the form of polymeric coatings including PEG, PLGA, Pluronic F127, etc., and a combination of more than one polymer and other forms [17–19]. In the case of bone cancer therapy and regeneration, BP has been applied in combination with 3D bone scaffolds, hydrogels, and fibrous scaffolds. A pioneering study has reported the design of a BPNS-coated 3D-printed bioactive glass (BG) scaffold for osteosarcoma and bone regeneration. The nanosheets were coated on the scaffolds through dip-coating without using any polymer and the coating improved the biomineralization and also eradicated the cancerous cells through photothermal therapy [12]. Another study took advantage of electrostatic interactions between BP and graphene oxide mixture and positively charged poly(propylene fumarate) to yield a multifunctional scaffold [20]. Other studies have incorporated BPNS inside diverse hydrogels and fibrous matrices and the results implied up-regulation of bone formation, biomineralization, etc. [21–24]. Recently, two studies have reported on the simultaneous bone cancer therapy and regeneration of BP nanosheets in two different frameworks—an injectable hydrogel and a 3D implantable scaffold [25,26]; one of which has incorporated doxorubicin and BP nanosheets with thermo-sensitive chitosan and β-Glycerol phosphate disodium salt hydrogel to take advantage of synergistic photothermal therapy and chemotherapy. The combinatory strategy resulted in the less side-effects related to doxorubicin plus more desirable anticancer activity against osteosarcoma and the degradation of BP realized biomineralization and stimulated bone tissue regeneration *in vitro* and *in vivo* [25]. The other one has reported the fabrication of a freeze-dried 3D scaffold composed of chitosan, hydroxypropyltrimethyl ammonium chloride chitosan, hydroxyapatite, and BP nanosheets. Interestingly, this study has taken advantage of BP's photothermal potential at two ranges ($\sim 42\ ^{\circ}C$ and $\leq 50\ ^{\circ}C$); the lower temperature has up-regulated the heat shock proteins and stimulated osteogenic gene expressions including alkaline phosphatase, osteocalcin, and collagen type I while the higher temperature was found to eradicate the cancerous cells without leaving behind negative effects on the healthy ones *in vitro* and *in vivo* [26]. However, it is still observable that most of these designs lack an efficient procedure to protect the nanosheets from oxidation.

The present study provides an innovative two-step strategy to synthesize a therapeutic-regenerative composite, starting from BPNSs, Pluronic F127 as surfactant and tetraethyl orthosilicate (TEOS), triethyl phosphate (TEP), and calcium chloride ($CaCl_2$) as a precursor of BG (Scheme 1). We adopted evaporation-induced self-assembly to synthesize BG-BP composites in an ethanol solution followed by exposure to microwave irradiation. The liquid crystals formed by Pluronic F127 during the drying process play a protective role and encapsulate BP in the hydrophobic core of micelles followed by the formation of BG moieties around them. Moreover, we performed microwave irradiation on the composite and turned the BPNSs into BP quantum dots (BPQDs) to come up with a theragenerative platform for bone cancer. The aims of this study were: (I) *In situ* synthesis and encapsulation of BG-BP, (II) assessment of the effects of Pluronic F127 and microwave irradiation on the physicochemical properties and cell compatibility of BG hybrid biomaterials, (III) evaluation of the effect of microwave on the physicochemical and biological properties of BP-incorporated hybrid composite, (IV) determination of the anticancer potential of nanocomposites and bare BP nanomaterials on the primary (osteosarcoma) and

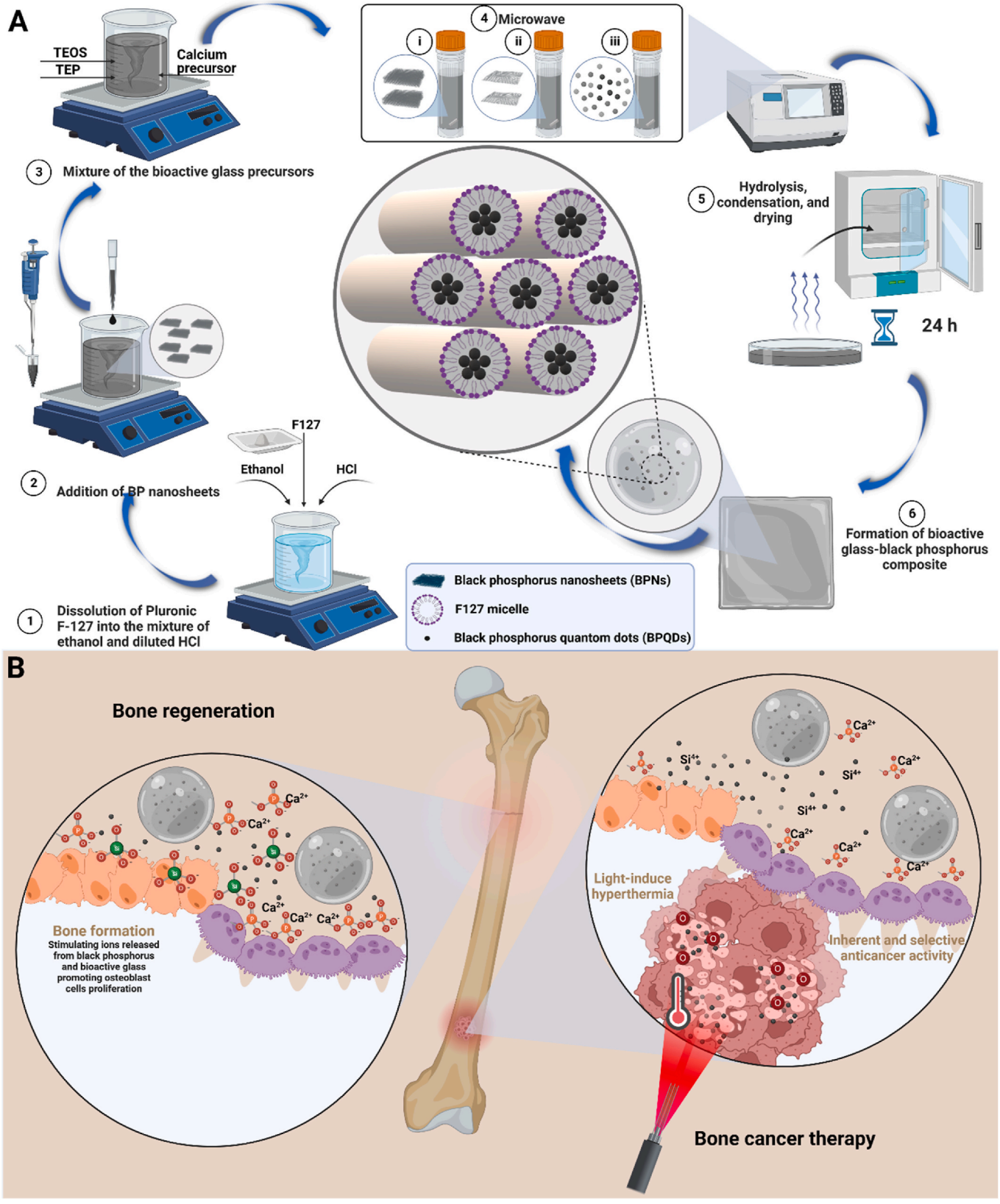

Scheme 1. Illustrations of BG-BP nanocomposites preparation and their theragenerative potential for bone cancer. (A) two-step synthetic strategy (sol-gel and microwave treatment) yielding F127-BG-BPQDs. **(B)** Theragenerative potential of the composites. Created with BioRender.com.

secondary (migration and invasion of breast and prostate cancer cells) bone cancers *in vitro* in terms of cell viability, PTT-induced anticancer activity, 2D migration, and 3D invasion assays, and (V) assessment of the nanocomposites regeneration ability through exposing to healthy human osteoblast and human mesenchymal stem cells in terms of cell viability, proliferation, and differentiation *in vitro*.

2. Materials and methods

2.1. Synthesis of bioactive glasses and composites

BPNSs were obtained through liquid phase exfoliation of BP in absolute ethanol and kept in an oxygen-free container in darkness to prevent potential oxidation [15]. A surfactant-assisted sol-gel method was adopted to synthesize the composites. Pluronic F127 (Sigma-Aldrich, Italy) was dissolved in a mixture of absolute ethanol and 0.1 M HCl followed by the addition of BPNSs dispersed in absolute ethanol. The final concentration of nanosheets in the synthesis mixture was 150 μg mL^{-1} [15]. Once a complete dispersion was obtained, the precursors of BG (SiO_2 60-CaO 30-P_2O_5 10 %), including TEOS, TEP, and $CaCl_2$ (Merck, Germany) were added one after another with an hour time interval between each precursor. The mixture was preserved at 50 °*C* for 3 h and then transferred into a microwave-assisted synthesis apparatus (Biotage Initiator). The solution was exposed to a two-step microwave irradiation for about 40 min [27]. Then, it was poured into a Petri dish and put into an oven at 40 °*C* to dry (Scheme 1(A)). To assess the effects of BP and microwave irradiation on the physicochemical properties of the composite, the following samples were produced: F127-BG, F127-BG-M, F127-BG-BPNS, F127-BG-BPQDs, where M refers to the microwave treatment, which is also responsible for the transformation of BPNSs into BPQDs.

2.2. Characterization

Assessment of structural properties of samples was performed through X-ray diffraction (XRD, Philips TW3710 (Netherlands)). A Bruker Avance Neo 500 spectrometer was adopted to record Solid State NMR (SSNMR) experiments; Larmor frequencies in the case of ^{29}Si and ^{31}P were 99.36 and 202.46 MHz in turn. For obtaining quantitative spectra a recycle delay of 300 s between two consecutive transients was used and 180 transients were accumulated for each spectrum. Total experiments related to SSNMR were performed at ambient temperature. A confocal Raman spectrometer (Labspec Aramis, from Horiba-Jobin Yvon, Edison, NJ, USA) was adopted to yield imaging in the mode of mapping with a 532 nm laser excitation source. The samples were fixed on the microscope stage and the resolution of x, y, and z was 10 ± 0.5 nm and 15 ± 1 nm, respectively, and after the collection of Raman data, they were converted into ASCII format. An in-house written code was then used to elaborate the Raman images in MATLAB. Fourier Transform Infrared spectroscopy-attenuated total reflection (FTIR-ATR) was carried out on a PerkinElmer instrument, model 1650. UV–vis absorption spectroscopy (Specord 210 Plus BU, FKV srl, Italy) was adopted to monitor the degradation degree of pristine BP and BP-incorporated samples. The morphological analyses were performed through scanning electron microscopy with energy dispersive spectroscopy (SEM-EDS, FEI Quanta 200 FEG) and Transmission electron microscopy (TEM, FEI Tecnai G2 Spirit TWIN).

2.3. Bioactivity

The *in vitro* biomineralization ability of the biomaterials was tested through simulated body fluid (SBF); the SBF was prepared based on the protocol developed by Kokubo et al. [28]. Powder samples were soaked into the SBF at a concentration of 3 mg mL^{-1} and put into an incubator at 37 °*C* for 14 days. During the test, the pH of each solution was measured at specific time intervals and reported as the mean of three samples ± the standard error. After 7 and 14 days, the solution was removed and the powder was rinsed with deionized water. Then they were transferred into an oven and dried at 40 °*C* for 24 h. The assessment of surface topography and compositional studies were performed through the SEM equipped with EDS. The structural and chemical bonding of newly formed precipitations on the samples were analyzed through XRD and FTIR-ATR, respectively. The concentration of SiO_4^{-4}, Ca^{2+}, and PO_4^{-3} ions during soaking period in SBF was measured for the samples through Inductively Coupled Plasma ICP, MS Thermo Fisher Scientific SpA (SN02597R).

2.4. In vitro degradation

The degradation rate of samples with and without BP was tested in deionized water for up to 21 days. A solution with 3 mg mL^{-1} was prepared from each sample and after 7, 14, and 21 days of soaking, the solution was withdrawn and the samples were dried in an oven at 40 °*C* for 24 h. The weight loss percentage was determined at each time interval based on the weight of the samples before immersion and represented as the mean of three samples ± the standard error. The pH of solutions was also measured on days 0, 3, 7, 10, 13, 17, and 21.

2.5. In vitro cell studies

2.5.1. In vitro cell viability

L929 cell viability was evaluated after 24 h of exposure to F127-BG-M, F127-BG, and BG alone at a concentration of 150 μg mL^{-1} using Alamar Blue assay to evaluate the effect of polymer and microwave treatment on the cells' viability *in vitro*. Specifically, L929 cells were seeded in a 96-well plate at a density of 1.0×10^4 viable cells/well. Cells seeded in plates without being exposed to any material were used as controls. After 24 h of seeding, the materials were put in contact with the cells and after 24 h of incubation, the culture medium was removed followed by direct addition of the AlamarBlue™ (Life Technologies, Italy) to each well and then preserved in an incubator for 4 h at 37 °C. A spectrophotometer (Victor X3, PerkinElmer, Milan – Italy (570 and 600 nm)) was adopted to measure the conversion of resazurin to resorufin. Quantitative data were confirmed through qualitative images obtained using an optical microscope (Motic™ AE31) at a magnification of 10X. For optical analysis, after 24 h of cell-materials interaction, each well was rinsed thrice with phosphate-buffered saline (PBS) 1X and cells were fixed with a solution of 4 % (w/v) paraformaldehyde (PFA) (Sigma-Aldrich) for 2h at room temperature. After cell fixation, the cells were rinsed three times with PBS 1X and observed with an optical microscope. Biological tests were also performed on an osteosarcoma-derived cell line (SAOS-2) to investigate the anticancer properties of F127-BG-M and F127-BG-BPQDs in terms of cell proliferation, oxidative stress species generation, and apoptosis induction. For cell proliferation, SAOS-2 cells were seeded in a 96-well plate at a density of 1.0×10^4 viable cells/well; after 24 h, the cells were treated with F127-BG-M and F127-BG-BPQDs at different concentrations ranging from 50 to 200 μg mL^{-1} for 24 and 72 h. The experiment was carried out using Alamar blue, as previously described, to determine which concentrations may cause cytotoxicity in the cells.

2.5.2. Oxidative stress

Oxidative stress effect was detected by measuring ROS through a fluorescent probe, 2,7-dichlorofluorescein diacetate (DCFH-DA, Sigma-Aldrich). Thus, to measure the ROS levels, SAOS-2 cells at a density of 1×10^4 viable cells/well were seeded in a 96-well plate for 24 h. After seeding, the cells were treated with F127-BG-M and F127-BG-BPQDs (150 μg mL^{-1}) for 24 h. Later, the cells were incubated for 60 min with 10 μM DCFH-DA in Hanks' Balanced Salt Solution without calcium or magnesium and phenol red (Gibco) containing 1 % fetal bovine serum (FBS) (heat-inactivated, 56 °C for 30 min, Sigma-Aldrich). Then, the cells were rinsed and incubated with the Fenton's reagent (H_2O_2/Fe^{2+} 2

mM) for 3 h at 37 °C. Finally, a fluorescent microplate reader was used to detect a 2′,7′-dichlorofluorescein signal. Increasing in the ATP levels is considered a requisite for the process of apoptotic cell death [29]; thus, the ATP content in SAOS-2 cells exposed to F127-BG-M and F127-BG-BPQDs for 72 h was quantified by using a commercial ATP Colorimetric Assay kit (Elabscience®) according to the manufacturer's instructions.

2.5.3. Cell apoptosis

To investigate the apoptotic effects of the materials on SAOS-2 cells, caspase-3 expression was evaluated by using confocal microscope analysis. Cells were cultured on glass slides at a density of 2×10^4 cells/slide within 24 h of seeding and were treated with F127-BG-M and F127-BG-BPQDs for 72 h. Later, the cells were rinsed with PBS and fixed with a solution of 4 % (w/v) PFA overnight at 4 °C; they were preserved in the exposure of 0.1 % Triton (Sigma-Aldrich) followed by being incubated in a solution (5 % (v/v) donkey serum in PBS) for another hour. The samples were rinsed three times in PBS and incubated with anti-caspase-3 antibody (1:100 dilutions, Abcam) at 4 °C overnight. Once the samples' rinsing had finished, Alexa Fluor 488 goat anti-rabbit secondary antibody (1:500, Abcam) was put into the samples' medium for incubation around 2 h at ambient temperature. The cells were then rinsed 2–3 times in PBS and then treated with phalloidin rhodamine working solution [Phalloidin-Atto 594 (1:200), Sigma-Aldrich] and incubated for 1 h. A concentration of 10 μg mL^{-1} was prepared from 4′,6-diamidino-2-phenylindole (DAPI) to stain the nuclei of cells at 37 °C for 10 min. The cells were observed using a confocal laser-scanning microscope at magnification 10X (Leica TCS SP8 confocal microscope, Germany). Caspase-3 expression, index of apoptosis, was confirmed by qualitative pictures of cells stained with annexin V-AF647. One of the most important advantages of this assay is to distinguish various stages of cell death thanks to Annexin V's ability to bind phosphatidylserine. Once the fixation stage was carried out, the Annexin V-AF647 kit (Elabscience®) was used to stain the cells and by performing confocal microscope analysis (Leica TCS sp8).

2.5.4. Cell migration and invasion

The cells were routinely cultured as follows: MCF7 in Eagle's Minimum Essential Medium supplemented with 10 % FBS, 2 mmol/L glutamine, and 10 μg mL^{-1} human insulin; MCF10A in Dulbecco Modified Eagle Medium (DMEM)/F12 supplemented with 5 % Horse Serum, 20 ng mL^{-1} Epidermal growth factor, 0.5 μg mL^{-1} hydrocortisone, 100 ng mL^{-1} Cholera toxin, and 10 μg mL^{-1} insulin; MDA-MB-231 in DMEM supplemented with 10 % FBS and 2 mmol/L glutamine; and PC3 in DMEM/F12 supplemented with 10 % FBS and 2 mmol/L glutamine. The cells were cultured at 37 °C in a humidified 5 % CO_2 atmosphere. All the precursors were provided by Thermo Fisher Scientific.

Seeding and culturing of MCF7 (8×10^3/well) or MCF10A cells (9×10^3/well) were performed onto 96-well plates. After 24 h, the cells were exposed to BPNSs and BPQDs at concentrations of 0.5, 1, 5, 10, and 25 μg mL^{-1} up to 72 h. The MTT solution was prepared at the concentration of 0.5 mg mL^{-1} and added to the cell culture medium for 4 h at 37 °C to perform cell viability of breast cancer and healthy cells being contacted with the BP nanomaterials. Next, the precipitated formazan crystals were dissolved through the addition of DMSO (100 μL/well) followed by incubation for 30 min. Finally, absorbances were determined through a plate reader at 570 nm (Cytation 3 BioTek Instruments, Winooski, VT, USA). Of note, the experiments were performed through three independent sets in quadruplicate.

A scratch-wound assay was performed to assess the 2D migration behavior of different cancer cell lines (SAOS-2, human osteoblasts (HOB), MDA-MB-231, MCF-7, MCF-10, and PC-3) in the presence of bare BP nanomaterials and the composites *in vitro*. Cells with nearly 80 % confluence were seeded into 12-well plates. To prevent further growth of the confluent cells, a proliferation inhibitor was added before applying the scratches. The scratches were performed using a sterile pipette tip (p200); to ensure recording of a similar scratch per each well, a blank line perpendicular to the prime one was applied on the well's bottom position. PBS was used to remove the dead cells by washing and then the conditioned medium was added to each well. The closure of the wound was monitored carefully and the related images were taken using AxioVision inverted microscope (Carl Zeiss Micro Imaging GmbH) after 4 and 24 h. Four replicates were taken for each sample, and the results were based on the mean.

Assessment of cell invasion assay was performed using a transwell chamber (Merck, Darmstadt, Germany). The seeding of MDA-MB-231, MCF7, and MCF10A cells was carried out in 6-well tissue culture plates (5×10^5 cells/well) and preserved for 24 h at 37 °C. The cells were then non-treated or treated with 0.1 μg mL^{-1} of BPNSs or BPQDs for another 24 h. At the end of this time, dilution of Matrigel (Merck, Darmstadt, Germany) was carried out using a serum-free medium to yield a solution with a concentration of 5 mg mL^{-1} with serum-free medium. The medium from 6-well culture plates was recovered (6-well recovered medium) and cells were detached and seeded to a final density of 8×10^4/well to the upper part of the transwell chamber in serum-free medium supplemented with 0.1 μg mL^{-1} of BPNSs or BPQDs. In the lower chamber, the 6-well recovered medium is served and is considered a source of chemoattractants. Next, the cells on the upside of the membrane were removed and the ones that invaded through the Matrigel were fixed using a 4 % paraformaldehyde solution. Eventually, an AxioVision inverted microscope (Carl Zeiss Micro Imaging GmbH) was adopted to determine the penetrated cells through the membrane.

2.5.5. In vitro osteogenic differentiation

Bone regenerative properties of F127-BG-M and F127-BG-BPQDs were tested both on HOB proliferation (AlamarBlue assay) and human mesenchymal stem cell (hMSC), in terms of cell viability (AlamarBlue assay at days 1,3,7 and 14) and osteogenic differentiation; assessment has been made on the expression of early Alkaline phosphatase (ALP) and later Osteopontin (OPN) and osteocalcin (OCN) signals. The ALP activity was determined using a SensoLyte pNPP ALP assay kit (ANASPEC, Milano, Italy) up to 14 days of incubation. In the case of OPN and OCN, their levels were also measured by immunocytochemistry analysis (cell density = 2×10^4 cells/well in a 48 multiwell plate) after 14 days. The samples were rinsed three times, permeabilized with 0.5 % Triton X-100, and then fixed in formalin for this purpose. Following a PBS wash, a 5 % BSA (bovine serum albumin) and 0.1 % Triton X-100 in Dulbecco's Phosphate Buffered Saline (DPBS) protein solution were added to the samples. The solution was removed after 30 min at 37 °C, and the samples were then treated for 1 h at 37 °C with rabbit osteopontin polyclonal antibody (1:50) and anti-osteocalcin antibody (Abcam) at a 1:200 dilutions in a solution of 5 % BSA and 0.1 % Triton X-100 in DPBS. Later, the samples were rinsed and treated with goat Rodhamine conjugated anti-rabbit secondary antibody (1:500, Abcam), Alexa Fluor 488 conjugated phalloidin (1:200 dilutions, Sigma-Aldrich) and DAPI, as described above. Finally, the samples were rinsed and analyzed using a fluorescence microscope (JuLI™ Stage, NanoEntek).

2.6. Statistical analysis

The statistical analysis of present study was performed through Graph Pad Prism 9 (La Jolla, CA, USA) software by one-way analysis of variance with the levels of statistical significance of ($^*P < 0.05$, $^{**}P < 0.01$, $^{***}P < 0.001$, $^{****}P < 0.0001$).

3. Results and discussion

3.1. Effects of microwave treatment and surfactant (F127) on bioglasses

BG samples prepared with and without F127 (F127-BG and BG, respectively) and treated with microwave (F127-BG-M and BG-M) were characterized by physical and chemical analyses. Moreover, the

samples' cell compatibility was tested against the fibroblast L929 cell line. Figs. 1 and 2 contain information regarding the structural, chemical, morphological, and biological properties of the different samples. The XRD patterns of samples with and without Pluronic F127 and microwave treatment are reported in Fig. 1(A). A wide peak is observed in all diffractograms in the region 2 Theta = 20–30°, due to amorphous silica [30,31]. The effects of F127 and microwave treatment are here observable; the samples without F127 have seen the formation of calcium chloride hydroxide (JCPDS 96-900-7716) as the main phase and some other phases. Notably, the peaks of F127-BG were weaker and wider than those of the samples without F127. Since the only difference between these samples was the presence of F127, the surfactant may restrict the interaction of ions during the evaporation-induced self--assembly process. F127 as a non-ionic surfactant contains a hydrophobic head with two hydrophilic tails [32]; the surfactant molecules could decrease the re-crystallization and growth of calcium chloride hydroxide nanoparticles. The microwave treatment to BG induced the formation of some other phases, as the result of increasing the kinetics of ion interactions. Microwave-assisted synthesis technique is a green technique adopting electromagnetic waves to accelerate and facilitate reactions. The applied alternating electric field in the process results in the orientation of polar molecules and any ion in the synthesis medium. Rotation, friction, and collision of these molecules are the main reasons for increasing the heat. The constant fluctuation of the synthesis medium provides an environment where the ions are more likely to interact with one another [33]. The effect of microwave treatment is evident from the comparison between the XRD patterns of samples F127-BG and F127-BG-M. Two sharp peaks appeared after the treatment, attributed to calcium oxide and carbonated hydroxyapatite (JCPDS 96-900-3555) as indexed in Fig. 1(A).

The morphological analysis obtained from TEM is shown in Fig. 1(B-E) and the aggregation processes occurring for the different samples were sketched below each micrograph. The micrographs indicate that a low amount of precipitates formed throughout the F127-BG composite without treatment, while the microwave irradiation caused the formation of some particles. Samples without F127 show a particle content much larger than samples containing F127. The probable reason for these findings resides in the fact that F127 decelerated the accumulation and growth of nanoparticles, while the irradiation enhanced the kinetics of the reaction, not only increasing the particles' size but also their crystallinity. The nucleation and growth have occurred here through three steps. The inorganic precursors including TEOS and TEP underwent hydrolysis and condensation first in the presence of F127 and HCl. As evaporation gradually took place, the concentration of HCl and F127 increased. The former increases the reaction kinetics, while the polymer has the potential to decrease the interaction of inorganic species. Notably, a rise in acid concentration causes the protonation of F127 surfactant molecules, resulting in the production of liquid crystals [34]. Second, the inorganic species—SiO_4, Ca^{2+}, and PO_4^{3-}—formed small clusters and dimers, and the last step was the coalescence of these clusters which formed the particles. In the case of the F127-BG sample, the initial clusters accumulated between the PEO chains of surfactant molecules and the hydrophilic tails prevented more collision of them (Fig. 1(B)). Since the microwave treatment increases the collision and interaction of ions through the applied electromagnetic waves, it was observed that the F127-BG-M yielded some precipitation through the structure (Fig. 1(C)). The effect of polymer on the particle size is more prominent in Fig. 1(D and E); in the absence of surfactant molecules, the ions could easily interact with each other and form bigger particles, and the microwave reinforced the growth kinetics even more.

Data on the functional groups present in the samples was obtained from ATR-FTIR spectra shown in Fig. 1(F). The peaks located at 806 and 1053 cm^{-1} represent symmetric and asymmetric stretching vibrations occurring between oxygen and silicon atoms (Si–O and Si–O–Si (ν_{SiO})) [35]. The bands at about 1648 and 3400 cm^{-1} correspond to the bending and stretching vibrations of hydroxide groups existing in the structure and/or absorbed from the atmosphere, respectively [36]. The signal observed at 905 cm^{-1} is attributed to free silanol groups [31]. The presence of F127 is evident from the signals in the spectral regions between 1300 and 1400 cm^{-1} and between 2800 and 2900 cm^{-1}. The

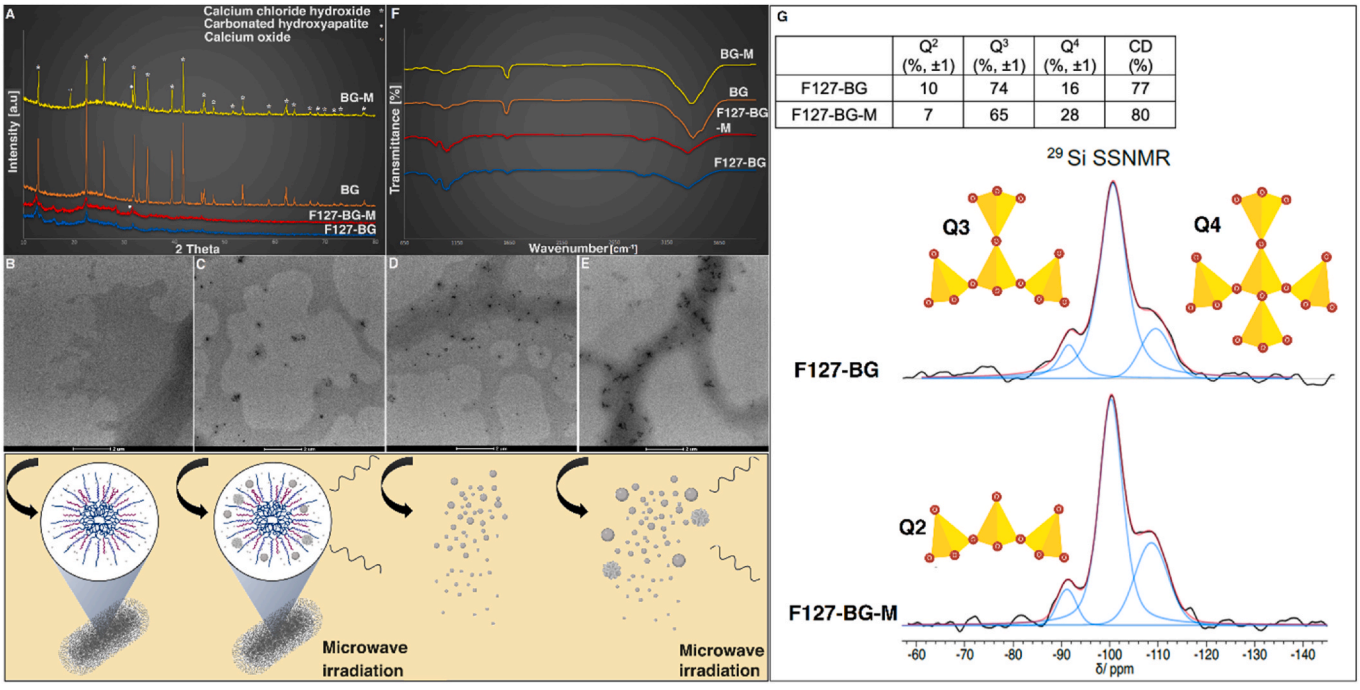

	Q^2 (%, ±1)	Q^3 (%, ±1)	Q^4 (%, ±1)	CD (%)
F127-BG	10	74	16	77
F127-BG-M	7	65	28	80

Fig. 1. Effects of F127 and microwave treatment on the structural, topographical, and chemical properties of BG. (A) XRD; TEM micrographs of **(B)** F127-BG, **(C)** F127-BG-M, **(D)** BG, and **(E)** BG-M; possible mechanism of action taking place during the synthesis procedure of each sample is indicated right below each micrograph. **(F)** ATR-FTIR spectra of samples. **(G)** ^{29}Si SSNMR spectra (DE-MAS) of F127-BG and F127-BG-M. The table reports the signal relative areas and the condensation degree (CD) values, as obtained from spectral fitting.

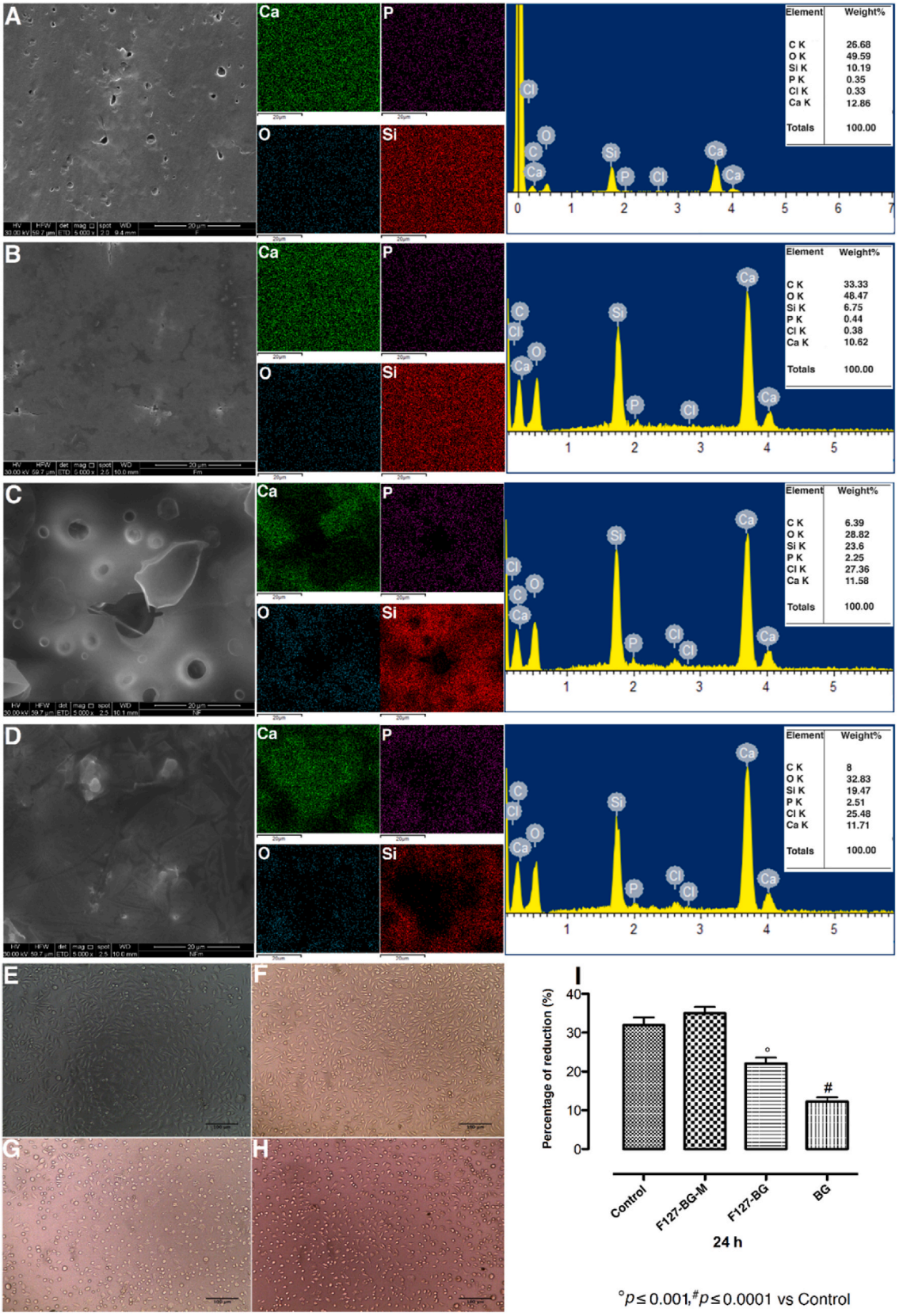

Fig. 2. Effect of F127 and microwave on the topography, structure, and cell viability of the samples. SEM micrographs, elemental mapping, and EDX analyses of **(A)** F127-BG, (**B**) F127-BG-M, (**C**) BG, and (**D**) BG-M. Micrographs taken from **(E)** fibroblast cells (control) being contacted with **(F)** F127-BG-M, **(G)** F127-BG, and **(H)** BG samples after 24 h. (**I**) Cell viability (% of control) of samples after 24 h against L929 fibroblast cells.

former represents stretching vibrations of —C—H bonds and the peaks at 1350 and 1420 cm^{-1} are related to stretching and bending vibrations that occurred between —C—H, $–CH_2$, and $–CH_3$, respectively [30,31].

Information on the structure of the silicate network of BG was obtained from quantitative ^{29}Si SSNMR spectra, shown in Fig. 1(G). ^{29}Si chemical shift is very sensitive to the local structure around silicon atoms. In particular, the ^{29}Si SSNMR spectra of both F127-BG and F127-BG-M clearly show three signals at −108, −100 and −91 ppm, ascribable to fully condensed $Si(OSi)_4$ silicon atoms, commonly indicated as Q^4 (with 4 being the number of Si–*O*–Si bonds), and to Q^3 ($Si(OSi)_3OH$) and Q^2 ($Si(OSi)_2(OH)_2$) sites, respectively. By performing a spectral fitting, it was possible to quantify the areas underlying the signals, directly proportional to the amount of the different silicon species, and the condensation degree (CD = 100 $(2Q^2+3Q^3+4Q^4)/(4(Q^2+Q^3+Q^4))$, where Q^i here indicates the area of the corresponding signal of the silicate network. The prominent silicon structural unit in F127-BG is Q^3, with a network CD of 77 %. When the microwave treatment is applied, the ^{29}Si SSNMR spectrum shows a decrease in the partially condensed Q^3 and Q^2 sites, with a corresponding increase in the fully condensed Q^4 species and the network CD (CD = 80 %) (Fig. 1(G)). Improvement in the network connectivity could arise from the effect of the microwave treatment on the reaction kinetics, which improved the condensation rate of the silica precursor. The decrease of the silanol groups can affect the physicochemical and biological properties of the material. Silanol groups can interact with the biological medium and for example, a higher bioactivity rate for bone tissue regeneration was observed when the proportion of these groups was higher [37,38].

One of the bottlenecks of BG-based hybrid materials is the diffusion and distribution of calcium ions throughout the hybrid's structure. It has already been reported that when calcium precursors including calcium chloride and calcium nitrate are used, a heat treatment above 400 °*C* is required for diffusion of calcium through the BG network. This is problematic in the case of BG hybrid materials which have an organic phase inside and cannot be calcined [39,40]. If the calcium is not incorporated in the BG structure, it can be suddenly released, thus inducing cytotoxicity [41]. On the other hand, using calcium alkoxides can be considered as an alternative option to introduce the calcium ions in the BG structure at room temperature. However, calcium alkoxides have a very high hydrolysis and condensation rate leading to inhomogeneous calcium distribution which is not suitable in terms of biomedical engineering [40]. Therefore, homogeneous distribution and controlled calcium release are of great importance in BG-based hybrid materials. Different approaches have been taken to stabilize calcium inside the BG structure for biomedical engineering like using various calcium precursors and polymers to turn the hybrid into chemically stable biomaterial. Aslankoohi et al. [42] developed a hybrid structure composed of L-phenylalanine-based poly(ester amide) and BG; the hybrid class was mentioned as type I, belonging to the groups of materials in which the hybrid is formed thanks to weak van der Waals, hydrogen, or electrostatic bonds. Calcium ethoxide was used as the precursor and the final product was found to form hydroxyapatite when soaked into SBF and supported the growth and proliferation of mesenchymal stem cells. Bossard et al. [43] have proposed a new viewpoint on calcium incorporation in the bioactive glass structure and adopted calcium hydroxide as the precursor. During the synthesis process, the pH of the medium was higher than the isoelectric point of silicic acid resulting in the deprotonation of silanol groups (SiO^-) that can weakly coordinate calcium ions ($[SiO–Ca]^+$). The benefits of calcium hydroxide as an alternative precursor were reproducibility, low cost, and commercialization potential. Another approach to releasing calcium ions in a sustained manner was to incorporate water-soluble calcium chloride into a hybrid scaffold, the introduction of 5 and 10 % was observed to stimulate apatite formation through supersaturation of the SBF [44].

The topography of samples with elemental analyses and cell viability against fibroblast cells are shown in Fig. 2. The elemental mapping has been taken to assess the distribution of the ions over the surface of the samples. The micrographs from **A-D** belong to F127-BG, F127-BG-M, BG, and BG-M samples in turn and the elemental mapping plus the EDX of each sample is indicated beside of it. The surface of F127-containing samples is integrated and homogeneous distribution of all ions throughout the surface is visible. The EDX has recorded 6 elements in the structure: Ca, Si, P, C, O, and Cl. Making a comparison between the elemental maps of BG and BG-M, it is visible that the microwave treatment did not affect the distribution of ions. Speaking of topography, our observations showed that the surface morphology was not significantly affected by the microwave treatment. On the other hand, the maps of samples with F127 show a more homogeneous elemental distribution than those without F127. Moreover, the F127-BG sample has an integrated surface with less porosity compared to the counterpart without the polymer. It is known that in acidic media, Pluronic F127 molecules are protonated, followed by being self-assembled based on the concentration of surfactant. The hexagonal 2D liquid crystals formed all over the structure acted as a scaffold and all the ions were absorbed and entrapped among the hydrophilic poly(ethylene oxide) (PEO) chains homogeneously. We also assessed the effect of F127 and microwave irradiation on the cell viability in BG against L929 fibroblast cells up to 24 h and the quantitative and qualitative results are indicated in Fig. 2 (E-I). The micrographs were taken after 24 h; round-like cells are visible for the samples without being treated with microwave and without F127. Notably, this sample showed the highest cytotoxicity among all because the polymer acts as a barrier against the burst release of inorganic ions. Moreover, F127-BG-M showed higher cell viability than the non-treated sample proving the effect of microwave on the chemical stability of the material.

3.2. *Black phosphorus-encapsulated F127 composite bioglasses*

BP has recently received great attention in biomedicine thanks to the variety of biomedical applications—cancer therapy, tissue regeneration, antibacterial activity, etc. [15,45,46]. This material is light-responsive and capable of inducing photothermal and photodynamic therapies while intrinsically can show selective anticancer activity without being triggered by an external light source [13,15]. One of the most important challenges in the use of this material is its high tendency to oxidation when being in contact with aqueous media and/or oxygen, weakening the optical properties [17]. Therefore, considerable attention has been given to designing synthesis routes during which BP does not undergo oxidation. One of the earliest approaches taken was to apply polyethylene glycol and polyethylene glycol-amine to stabilize BP in biological media, but the material has undergone oxidation [47,48]. Various polymers were used to encapsulate either BPNSs or BPQDs and applied successfully in biomedicine [19]. For bone cancer therapy and regeneration, BP has been incorporated into/onto electrospun scaffolds [24], hydrogels [49], and 3D-printed scaffolds [12]. Although the results were promising and revealed bone cancer therapy followed by regeneration, most of these synthesis approaches are complex and time-consuming. The present study adopted for the first time an easy but effective approach to come up with a theragenerative platform for bone cancer.

BP-encapsulated F127-BG composites, with and without microwave treatment, were characterized using TEM, SSNMR, and Raman spectroscopies (Figs. 3 and 4). BPNS is generally known to have a sheet size in the range of 150–200 nm with irregular morphology [15]. In Fig. 3 (A), a BP nanosheet is observable while after the microwave treatment, tiny dots (~5 nm) were obtained (Fig. 3(B and C)). The nanosheets were used as the precursor in ethanol and the process is depicted in Fig. 3(D), where the composite was dispersed in the solvent (**I**) and the treatment got started (**II**). The homogeneous heat applied through microwave irradiation causes the ethanol molecules to gradually intercalate through the layers and delaminate them into single sheet layers (**III**) at the first step (70 °*C*). Applying the second cycle was synchronized with an increase in the internal pressure exerted from the vaporization of

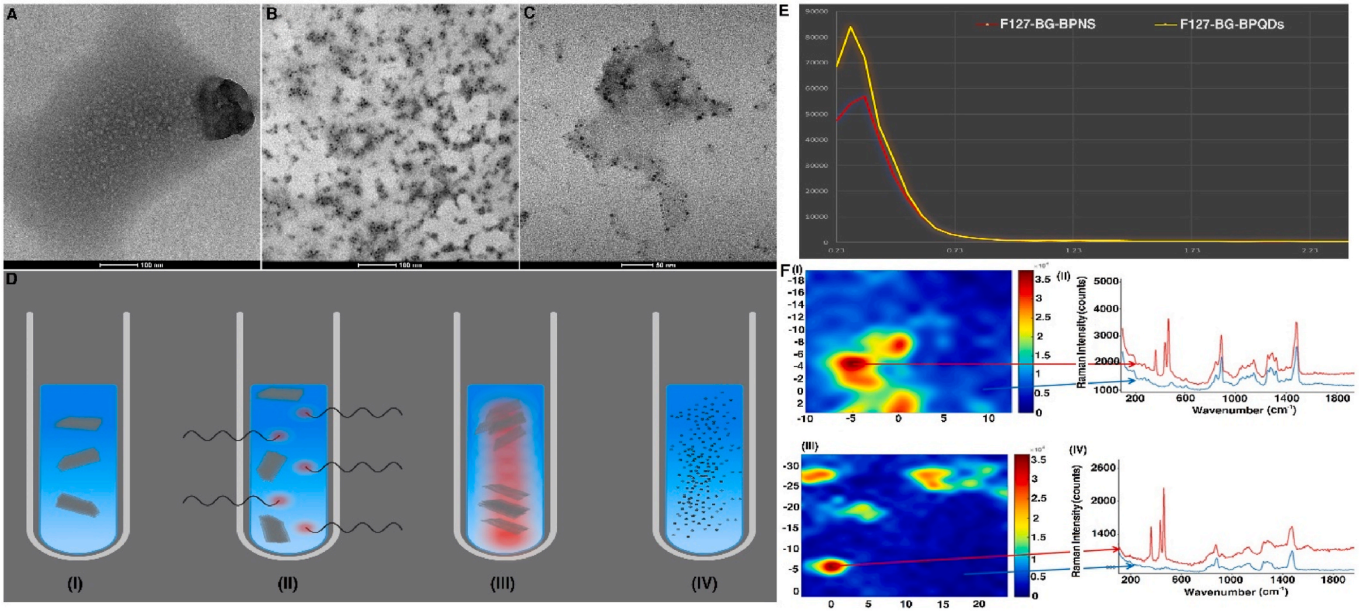

Fig. 3. Effect of microwave treatment on the BP-encapsulated F127-BG composite. TEM micrographs of **(A)** F127-BG-BPNS and **(B** and **C)** F127-BG-BPQDs. **(D)** A schematic illustration of the process of microwave treatment applied to yield BPQDs inside of the composite. Created with BioRender.com. **(E)** low-angle XRD of F127-BG-BPNS and F127-BG-BPQDs. **(F)** Raman images of F127-BG-BPNS **(I)** F127-BG-BPQDs **(III)**. Raman spectra were collected in different map points: F127-BG-BPNS **(II)** and F127-BG-BPQDs **(IV)**. The arrows indicate where the spectral collection was performed.

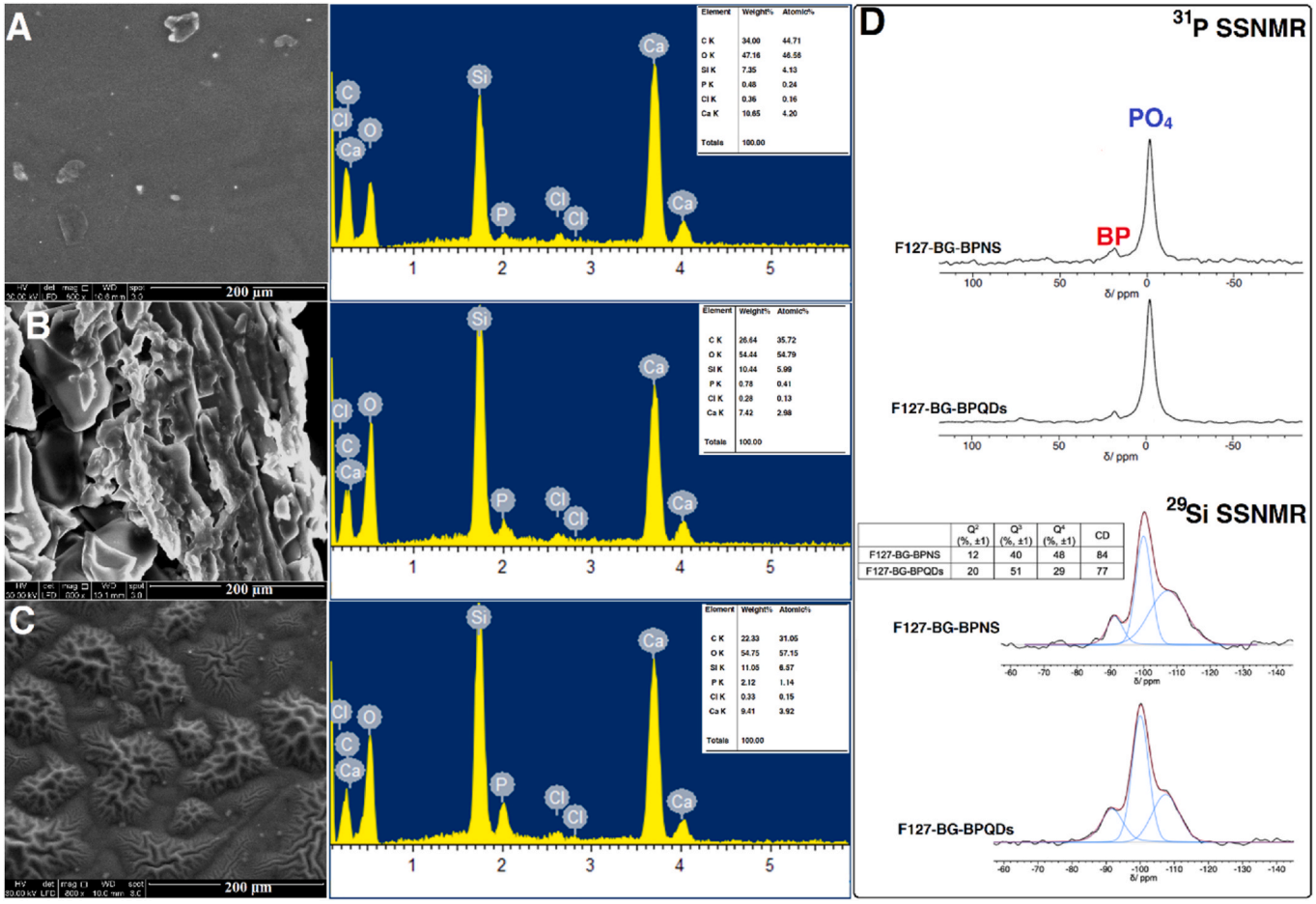

Fig. 4. Structural and elemental analyses of F127-BG-BPNS and F127-BG-BPQDs samples. SEM micrographs and EDX analysis of **(A)** F127-BG-M, **(B)** F127-BG-BPNS, and **(C)** F127-BG-BPQDs. **(D)** ^{31}P and ^{29}Si SSNMR (DE-MAS) spectra of F127-BG-BPNS and F127-BG-BPQDs samples.

ethanol; this pressure was reinforced further with the rotor shear force applied by the apparatus and both led to a significant decrease in the van der Waals interaction and formation of BPQDs throughout the F127-BG structure (**IV**). We verified the effect of microwave irradiation on the oxidation state of BP by recording quantitative ^{31}P SSNMR spectra on suspensions of BP before and after microwave treatment (Fig. S1, Supporting Information). In both spectra, it is evident the intense signal at 18.0 ppm arising from exfoliated BP and several weaker signals between −0.2 and 8.0 ppm due to oxidized phosphate and phosphite species [50]. From signal areas, it is possible to estimate that phosphorus atoms in the oxidized state constitute about 20 ± 5 % and 30 ± 5 % of the whole phosphorus amount, in BPQDs and BPNSs samples, respectively. This level of oxidation is often observed in samples of exfoliated BP since it is caused by manipulation procedures. These results indicate that the microwave irradiation by itself did not cause oxidation.

Low-angle XRD was adopted to assess the effect of microwave and BP addition on the order of liquid crystals formed by F127. Evaporation-induced self-assembly, which was applied to synthesize the hybrid in the present study, mixes the traditional sol-gel chemistry and the surfactant-assisted sol-gel approaches. The solution contains an inorganic precursor, directing agent or surfactant, and other types of additives which turn from diluted to concentrated ones as the volume of solution decreases due to drying. The F127, which was used here, forms surfactant molecules in the solution after dissolution, and once the solution is poured on a Petri dish, step by step the concentration of F127 goes higher and higher leading to the formation of liquid crystals and the final product is an inorganic-organic hybrid. We took advantage of the surfactant molecules (F127) to encapsulate the BP which has a hydrophobic nature [51]. Generally speaking, the XRD patterns of the mesoporous materials with or without calcination show some reflections at low angles and the peaks represent the periodical phase related to the liquid crystals (not-calcined) or pores (calcined) [52]. Fig. 3(E) shows the low-angle XRD patterns of F127-BG-BPNSs and F127-BG-BPQDs, where there is only one peak visible indexed to the (110) related to a 3D Im*3m* lattice for both samples but different in intensity. The higher intensity means a larger order in the liquid crystals phase [52]. As observed in the TEM micrographs (Fig. 3 (A-C)), the microwave irradiation led to the formation of BPQDs which can be embedded inside of the liquid crystals, while the BPNSs are approximately between 150 and 200 nm which are too large and so they break up the order of liquid crystals. It can be concluded that the BPQDs after microwave treatment were successfully encapsulated inside the F127-BG hybrid biomaterial.

The BP distribution in the BG matrix was evaluated by Raman mapping experiments before and after the microwave treatment. Numerous maps were collected in several areas of the samples in the spectral range 100–2000 cm^{-1} and representative results are reported in Fig. 3(G). Fig. 3(G)(II) and Fig. 3(G)(IV) show the Raman spectra collected at different locations within the mapped areas. The characteristic BP peaks are evident at 363 cm^{-1} (out-of-plane mode, Ag^1), 440 cm^{-1} (in-plane mode, B_{2g}) and 467 cm^{-1} (in-plane mode, A_g^2) [53] in selected regions of the maps (red traces in Fig. 3((G)II and **IV**) while in other areas the spectra show only the spectral pattern distinctive of the BG matrix (blue traces in Fig. 3((G)II and **IV**). The Raman images (Fig. 3 ((G)I and **III**), reconstructed by considering the intensity of the BP peak at 468 cm^{-1}, display the presence of BP clusters in the BG with an approximate size of 5 μm. These phase-separated domains can aggregate with each other or may remain isolated. The structure of samples containing BP before and after microwave treatment was further analyzed through SEM equipped with EDS (Fig. 4(A-C)) and SSNMR (Fig. 4(D)). The surface of the F127-BG-M sample is integrated and mostly smooth, while the addition of BPNS seems to disintegrate the uniformity, probably because nanosheets aggregate to form bigger particles and partially disrupt the integrity of the composite. In the case of F127-BG-BPQDs, the surface shows some wrinkles, but it is still integrated. ^{31}P SSNMR spectra of F127-BG-BPNS and F127-BG-BPQDs samples (Fig. 4(D)) show the peak of exfoliated BP at 18 ppm, beside the intense signal due to phosphates of BG. The BP peak accounts for approximately 10 % of the total amount of phosphorus nuclei in the sample, in good agreement with what is expected based on the sample composition. In the case of F127-BG-BPQDs, the signal of BP is slightly less intense than for F127-BG-BPNS, but the difference is within the experimental uncertainty. ^{29}Si SSNMR spectra of both samples (Fig. 4(D)) show the same signals as those without BP, namely signals from Q^4, Q^3, and Q^2 sites, in a similar relative proportion. However, it can be noticed that, in the presence of BP, after the microwave treatment, the amount of Q^3 and Q^2 increases, and the condensation degree of the silicate network decreases (from 84 to 77 %).

3.3. Bioactivity and degradation in vitro

An ideal bone substitute is supposed to be biologically active having interaction with the surrounding medium. Bioactivity is the capability of the material to interact with the surrounding microenvironment. Here, it refers to the formation of carbonated calcium phosphate on the surface of the biomaterial, which can make interact with the host bone and prevent the biomaterial's loosening [54–56]. The bioactivity and degradation behavior of F127-BG, F127-BG-M, F127-BG-BPNSs, and F127-BG-BPQDs samples were evaluated *in vitro*, and the findings are shown in Figs. 5 and 6. The surface topography of F127-BG, F127-BG-M, F127-BG-BPNSs, and F127-BG-BPQDs after being soaked into SBF for 7 and 14 days were observed through SEM and also elementally analyzed with EDS. The EDS spectra were taken from the surface of each sample after 14 days. Moreover, Fig. 6(A-F) shows the results of the weight and pH change of the samples in deionized water and SBF and the ATR of samples after 14 days of soaking into SBF. Scheme 2 shows the probable bioactivity mechanism taking place in each sample. The surface of F127-BG has experienced a bit of modification and shows some newly formed precipitate after 7 days, while a lower amount of precipitate is observed on the surface of F127-BG-M. Fig. 6(A and B) shows that F127-BG and F127-BG-M exhibit different weight loss and pH alterations in SBF as a result of the microwave treatment. During the early stages of soaking into SBF, F127-BG-M saw more weight loss than the non-treated counterpart and their pH change patterns were also contrary to each other; the pH of the non-treated sample decreased (from 7.4 to 7.25–7.3) while that of the other slightly increased (~7.46). The main reason for the alkalinization was related to the exchange of Ca^{2+} with H^+ ions in the medium which is generally observed for the BG and similar compositions [37,54,57]. However, for both samples, two phenomena have occurred: the exchange of Ca^{2+} with H^+ ions and the release of Cl^- ions. Both processes took place at the same time but the latter prevailed in the early stages of F127-BG. This was the case up to the third day and the pH trend changed from acidic to alkaline showing the effect of the former process. On the other hand, in F127-BG-M the Cl^- release was controlled at first, and after 3 days, the ions started to release and turned the pH toward acidity for up to 7 days and then got stable. In Scheme 2 it can be seen that the general bioactivity mechanism occurred through four stages: (i) an ion exchange took place between the biomaterial and the medium and Ca^{2+} ions were replaced with H^+ ions. Then, (ii) silanol groups gradually formed and provided a position on which (iii) Ca^{2+}, Mg^{2+}, Na^+, K^+, and PO_4^{3-} ions could precipitate and form an amorphous layer. Finally, (iv) crystallization occurred in the deposited layer. The silanol groups in the structure of F127-BG and F127-BG-M were indicated differently from each other (Scheme 2). The concentrations of SiO_4^{4-}, Ca^{2+}, and PO_4^{3-} from F127-BG-M and F127-BG-BPQDs were measured through ICP at different time intervals up to 14 days (Fig. S2 in Supporting Information). It was observed that SiO_4^{4-} groups were released faster at the initial soaking period from the F127-BG-BPQDs than the one without BPQDS which can be related to the effect of quantum dots on the fully dense silicate groups by which these ions got liberated faster than the counterpart. However, from day 3–7, the concentration was decreased due to consumption of them attributed to the higher bioactivity rate of BPQDs-containing sample; the sample without

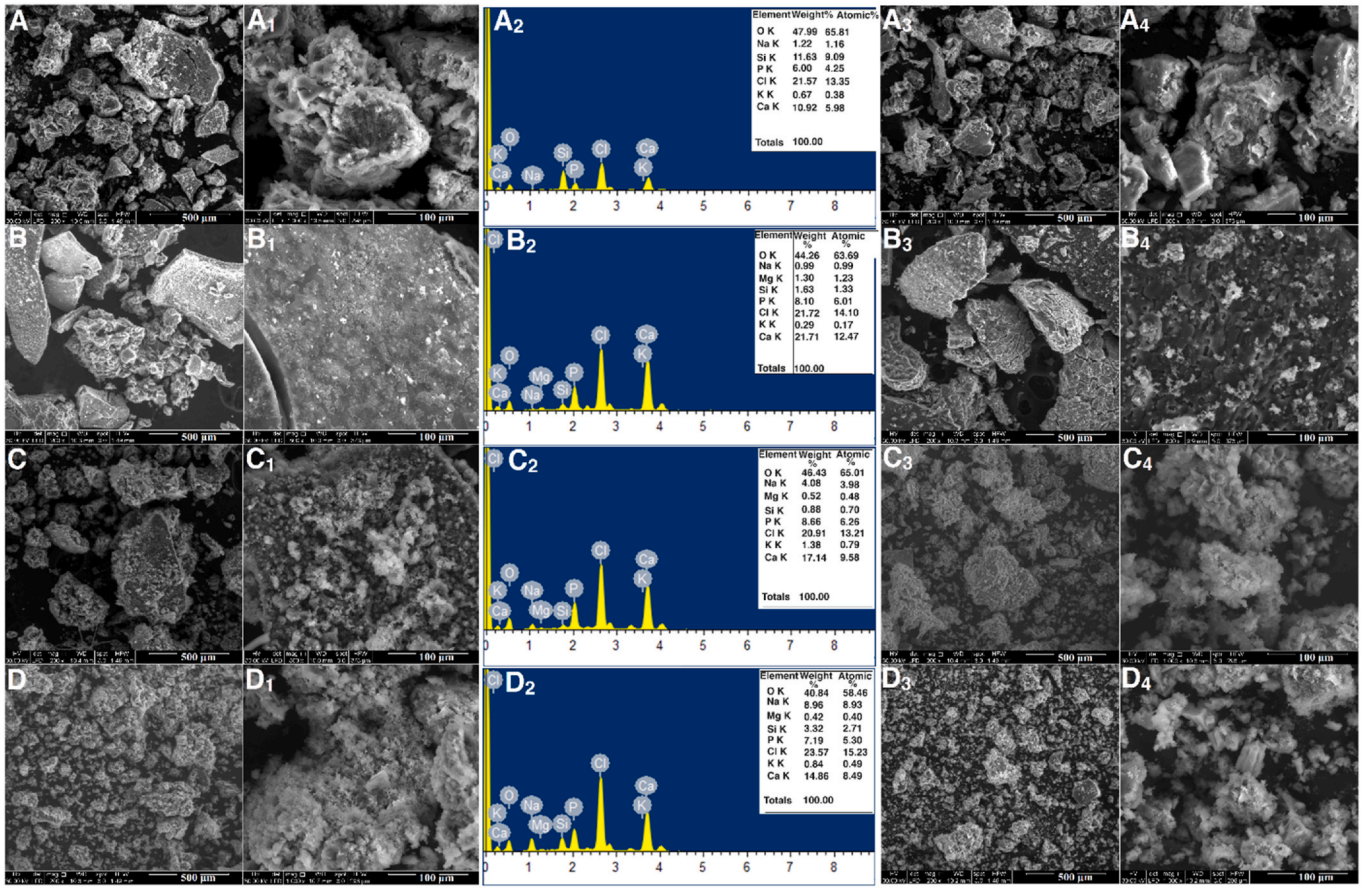

Fig. 5. ***In vitro*** **bioactivity assessment in SBF up to 14 days.** SEM micrographs and EDX analysis of the samples after 7 and 14 days: **(A-A$_4$)** F127-BG, **(B–B$_4$)** F127-BG-M, **(C–C$_4$)** F127-BG-BPNS, and **(D-D$_4$)** F127-BG-BPQDs. **A-C** and **A1-D1** micrographs were taken after 7 and 14 days, respectively. EDX analyses were performed on the sample surface after 14 days.

BPQDs has shown a continuous increase in silicate content up to 80 mg L^{-1} ^{29}Si SSNMR spectra in Fig. 1(G) showed that the relative amount of silanol groups (Q^2 and Q^3) in F127-BG is larger than in the sample treated with microwave (F127-BG-M). These silanol groups helped F127-BG to form some precipitate up to 7 days and faster than F127-BG-M. However, in the end, it was F127-BG-M that also quantitatively gained the most precipitation among all and even got 2 mg more weight (17 mg) than its initial starting weight (15 mg). The bioactivity mechanism for the samples containing BP was a bit different from the ones without BP. BP is known to degrade in the physiological medium to PO_4^{3-} groups which can be a precursor for calcium phosphate [58]. Ca^{2+} ions can be seen to be less in the BPQDs-containing sample than the counterpart (Fig. S2 in Supporting Information), which is in accordance with other results here, relating to the higher reactivity of this sample which consumed these ions and formed precipitation faster. Moreover, this is the case for the phosphate groups; these ions were constantly decreased for up to 7 days due to the release of phosphate from both the BPQDs and BG structure and then plateaued. Fig. 5(C-D) exhibits the surface of F127-BG-BPNSs and F127-BG-BPQDs (after microwave treatment) and the EDX spectra after 14 days. Both samples formed new precipitates in high amounts even after 7 days and our early observation showed that the sample with BPQDs had even more deposition after 7 days. Apart from the general bioactivity mechanism that was proposed for the samples without BP, these samples were endowed with BP as a booster for the bioactivity kinetics. As indicated in Scheme 2, BP released from the composite underwent degradation, thus producing PO_4^{3-} anions in the medium ready to interact with cations, mostly Ca^{2+}. This process increases the bioactivity kinetics culminating in the formation of new precipitates as indicated in the micrographs in lower magnifications (Fig. 5(C and D)). The microwave-treated sample contained quantum dots instead of nanosheets which is an advantage here because the BPQDs are more reactive than the layered nanosheets; once the nanosheets are exposed to a physiological medium, oxygen and water molecules attack their surface and results in the formation of PO_4^{3-} ions, but as the structure is layered, the interior layers remain intact until diffusion of water and oxygen or delamination of the layers takes place. On the other hand, the 5 nm BPQDs could undergo the oxidation process faster than the nanosheets and this is the reason why F127-BG-BPQDs had a faster bioactivity. Taking a glance at the pH change of these samples, the one with BPQDs showed an increase in the pH in the first 3 days attributed to the exchange of surface ions with the medium, as for F127-BG-M, but the pH got more alkaline than for F127-BG-M; this effect was caused by the release of quantum dots, which have been reported to turn the pH toward alkalinity [12]. The decrease in pH observed after three days is caused by the Cl^- ions as well. Then the trend of pH remained stable for the subsequent three days, due to the balance between the ions exchange and Cl^- release. Next, the pH gradually turned again toward higher values as the result of calcium phosphate deposition on the surface of the sample.

The functional groups present on the sample surface after 7 and 14 days of immersion into SBF were characterized by ATR-FTIR; the recorded spectra are shown in Fig. 6(C and D). The spectra taken after 7 days did not show a significant difference in the bands from those acquired on the samples before soaking. However, prolonging the immersion time up to 14 days was synchronized with the appearance of new peaks. In particular, a small but sharp peak has appeared in the spectra of all samples around 1260 cm^{-1} arising from the asymmetric and symmetric stretching of non-bridging oxygen atoms in the

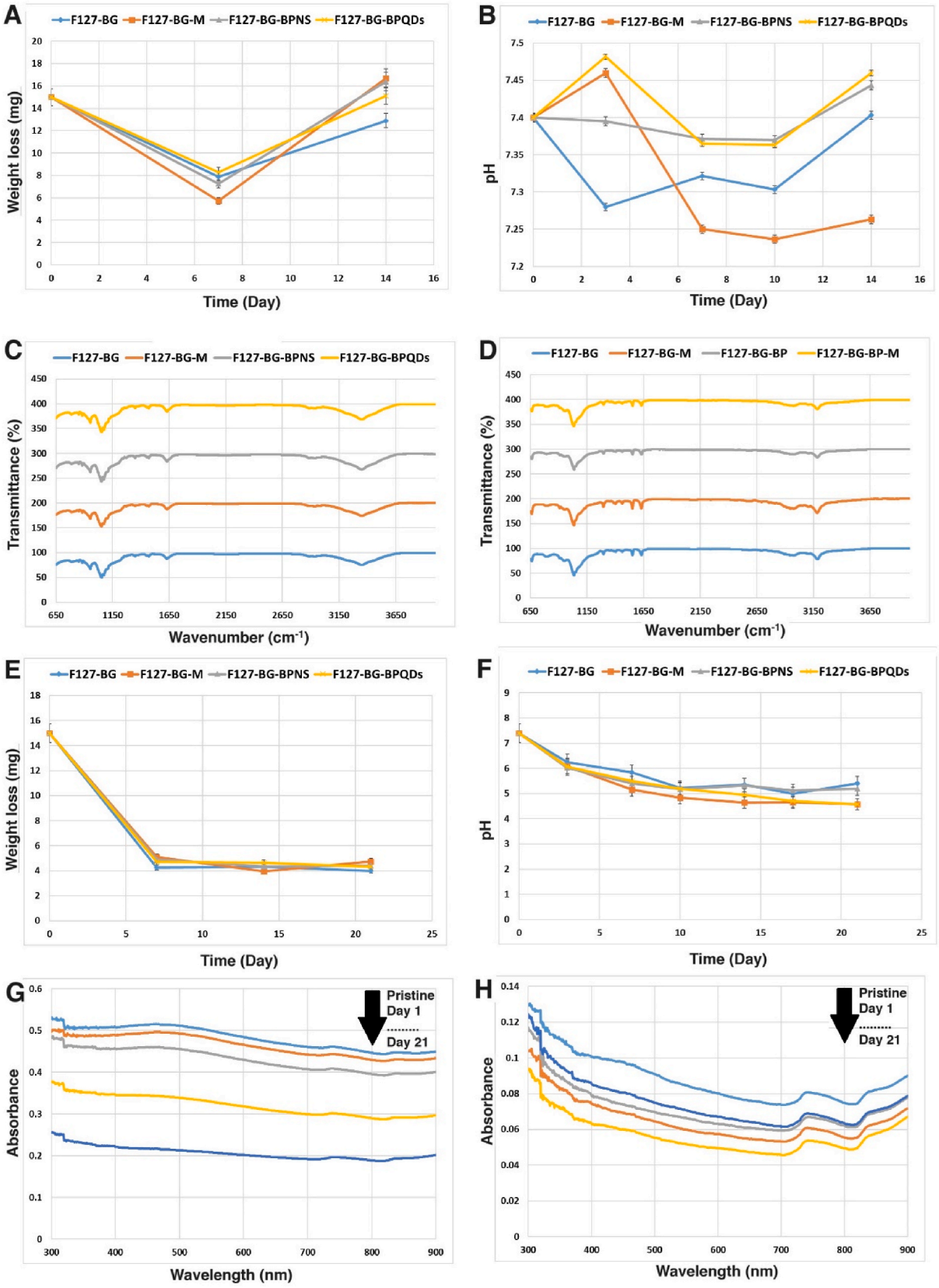

Fig. 6. Bioactivity and degradation rate *in vitro*. **(A)** Weight loss of samples in SBF up to 14 days. **(B)** pH change in SBF for 14 days. ATR-FTIR spectra of the samples **(C)** after 7 days and **(D)** after 14 days. **(E)** Degradation study performed in deionized water for 21 days. **(F)** pH changes during the soaking of samples into deionized water. UV–vis absorption spectra of **(G)** pristine BPQDs and **(H)** F127-BG-BPQDs dispersed in deionized water for 21 days indicating how oxidation affected the optical properties of BP nanomaterials during the soaking time.

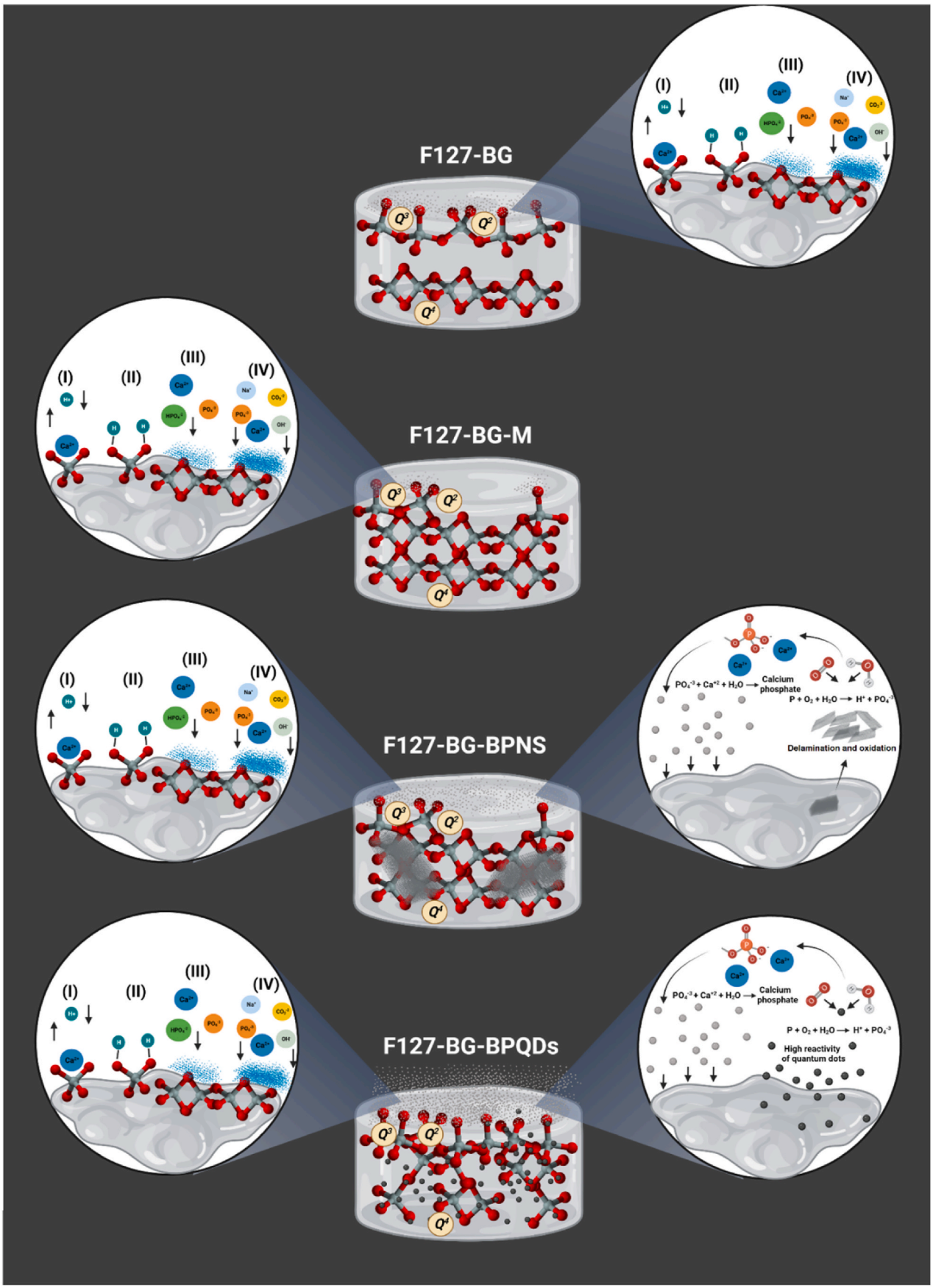

Scheme 2. Possible *in vitro* bioactivity mechanisms for the indicated samples. Created with BioRender.com.

phosphate groups [59]. Instead of the peak at 1053 cm^{-1}, due to stretching vibrations of silicon and oxygen atoms, a new band was observed at the lower wavenumber (1037 cm^{-1}), which can be assigned to the symmetric stretching mode of phosphate groups [60]. There was a band at 800 cm^{-1} in the spectrum of samples before immersion and this peak got a little intensified after soaking up to 14 days; it is ascribed to the Si–O–Ca groups with non-linking oxygen [61]. It is reported that the crystallization of hydroxyapatite is accompanied by the appearance of a shoulder around 650 cm^{-1} and the band at 660 cm^{-1} corresponds to the P–O resonance in the phosphate groups [60,62]. The two peaks at 1553 and 1631 cm^{-1} are related to carbon and oxygen resonance in CO_3^{2-}. SBF contains carbonate ions and they tend to substitute hydroxide ions (OH^-) in the lattice of hydroxyapatite and turn it into carbonated apatite [61].

The degradation behavior of F127-BG, F127-BG-M, F127-BG-BPNSs, and F127-BG-BPQDs was assessed in deionized water *in vitro* for up to 21 days and pH was monitored during this period; the obtained data are shown in Fig. 6(E and F). There are two trends visible in Fig. 6(E): a decrease in the weight of all samples up to 7 days, followed by a plateau for the rest of the degradation study. On the 7th day, there were differences among the samples and F127-BG-M was the one which showed the lowest weight loss, while F127-BG showed the highest. Continuing the test up to 14 days, slight changes in the weight loss were found: F127-BG-M underwent a decrease in its weight and then started to gain till the last time interval, whereas the other samples experienced a steady state with a small fluctuation in their degradation rate. Speaking of pH trends, PBS is different from SBF in ions type and concentration and here, the difference in pH changes of the samples compared to SBF is clear. At the initial immersion time, all samples experienced a continuous decrease in pH down to nearly 5 and then slowed down and became more stable. Since PBS lacks ionic species including Mg^{2+}, Ca^{2+}, and HCO^{-3} [63], the ion interaction the same as SBF does not occur, and the release of Cl^- prevailed the absorption of H^+ from the medium and led to the decrease in the pH. However, this trend has changed and the release of Ca^{+2} ions from the nanocomposite slowed down the trend and made a plateau.

One of the bottlenecks of BP nanomaterials is the oxidation in aqueous media accelerating the degradation rate and weakening the optical properties of BP. A simple way to monitor the degradation degree of BP is through UV–vis optical absorption [64,65]. Both pristine BPQDs and F127-BG-BPQDs were dispersed in deionized water (without deoxygenation) for up to 21 days and at different time intervals, the absorbance was measured in the range of 300–900 nm (Fig. 6(G and H)). The pristine BPQDs turned out to degrade gradually as expected reaching 58 % of the degradation degree after 21 days of dispersion in deionized water, whereas the composite showed a degradation degree of 38 % after the same time interval. This shows that the encapsulation of BPQDs into the F127-BG improved the BPQDs' stability, decreasing the degradation degree by 20 %. In addition, a very low degradation degree of BP in F127-BG-BPQDs was observed by comparing ^{31}P SSNMR spectra of the sample before and after being soaked in water for 3 days (Fig. S3 in Supporting Information). The spectra clearly show a decrease of the phosphates peak, ascribable to a partial dissolution of BG, while the intensity of the BP signals remains substantially the same, confirming the protective effect of the encapsulation.

Referring to the physicochemical and *in vitro* biological-related studies performed to reveal the effects of F127, BP, and microwave treatment on the nanocomposites, it was found that the microwave treatment could chemically improve the stability and bioactivity. Therefore, F127-BG-M and F127-BG-BPQDs were chosen as the optimized samples for cell-related studies *in vitro*.

3.4. Biological studies

In the first set of our biological studies, the effect of F127-BG-M and F127-BG-BPQDs on the growth rate of osteosarcoma cells (SAOS-2) was assessed *in vitro* for up to 72 h in static conditions. The assay was performed using Alamar blue to understand which concentration could be cytotoxic. The results are shown in Fig. 7(A). When F127-BG-M and F127-BG-BPQDs at concentrations ranging from 50 to 200 μg mL^{-1} were exposed to SAOS-2 cells, after 24 h, a general decrease in the cell viability of both groups was visible by increasing the concentration; however, the reduction was only 10–15 % and not statistically significant in most cases. Only for F127-BG-BPQDs with the 200 μg mL^{-1} concentration the cell viability difference compared to the control was statistically significant. Continuing the assay up to 72 h, significant differences in cell viability were observed for both F127-BG-M and F127-BG-BPQDs; the sample without quantum dots improved the cell viability up to 150 μg mL^{-1} and only 200 μg mL^{-1} caused a decrease in the viability, whereas the one containing BPQDs showed cytotoxic effect on the cells at 150 μg mL^{-1}. Since F127-BG-M (150 μg mL^{-1}) did not affect the cells negatively while the same concentration of F127-BG-BPQDs significantly prevented the growth of cells, the effect should be sought in the anticancer activity of BPQDs.

One of the most studied approaches in anticancer activity is based on ROS. ROS generated in a cancer cell beyond its tolerance induces apoptosis. Various agents responsive to light and/or ultrasound are assessed under the category of photodynamic and sonodynamic therapies [66]. Herein, ROS produced by F127-BG-M and F127-BG-BPQDs in the exposure of SAOS-2 cells without being triggered by NIR was determined after 24 h (Fig. 7(B)). Compared to the control, the samples almost tripled the ROS content which has the potential to activate various cell death pathways whereas our previous study on the anticancer potential of bare BP nanosheets against SAOS-2 cells showed two-folded increase in the ROS generated after 24 h [15]. Apoptosis is considered a programmed cell death process that can take place through endogenous and exogenous signals. Since apoptosis needs energy, it is directly related to ATP-dependent steps including activation of caspase, chromatin condensation, etc. It is important to mention that depletion of ATP is a sign that the cell has undergone necrotic rather than apoptotic death [29]. The ATP levels were measured when F127-BG-M and F127-BG-BPQDs had been exposed to the cells; the quantitative results are shown in Fig. 7(C). The sample without BPQDs was considered as the control since this sample at 150 μg mL^{-1} did not leave any negative effects on the viability of SAOS-2 cells, whereas the one with BPQDs showed an increase in the ATP levels nearly doubled as an index of apoptosis. Caspase-3 expression was assessed after 72 h for control (Fig. 7(D)), F127-BG-M ($\mathbf{D_1}$), and F127-BG-BPQDs ($\mathbf{D_2}$). The Caspase-3 expression was marked with a green signal in the SAOS-2 cells and the sample without BPQDs did not affect the cells and no green signal is visible in the sample's micrographs. However, BPQDs increased Caspase-3 expression as the index of apoptosis induced in the cells. Moreover, Annexin V staining was adopted to detect apoptotic cells, and the results are shown in Fig. 7(E-E_2). Similar to the control, the cells being exposed to F127-BG-M preserved their membrane integrity with a suitable spreading, whereas the ones treated with F127-BG-BPQDs underwent apoptosis and lost membrane integrity. A scheme is shown in Fig. 7(F) to propose a probable anticancer mechanism for F127-BG-BPQDs. Apart from photothermal and photodynamic therapies which adopt an external stimulus to induce hyperthermia and ROS generation, BP is known to induce anticancer activity intrinsically and selectively. It was proposed earlier that the nanosheets after being internalized into cancer cells undergo a fast degradation due to the higher metabolism rate and oxidative stress in these cells compared to healthy ones resulting in the production of phosphate anions, which increase the levels of intercellular protein phosphorylation that has different roles, among which triggering of cell death can be enumerated. Therefore, the higher degradation rate of BP nanosheets in different cancer cells resulted in apoptosis through G2/M phase arrest [13]. The selective anticancer ability and regenerative potential of BP nanosheets simultaneously were reported by our group. BP nanosheets could inhibit osteosarcoma cells' metabolic activity while stimulating the

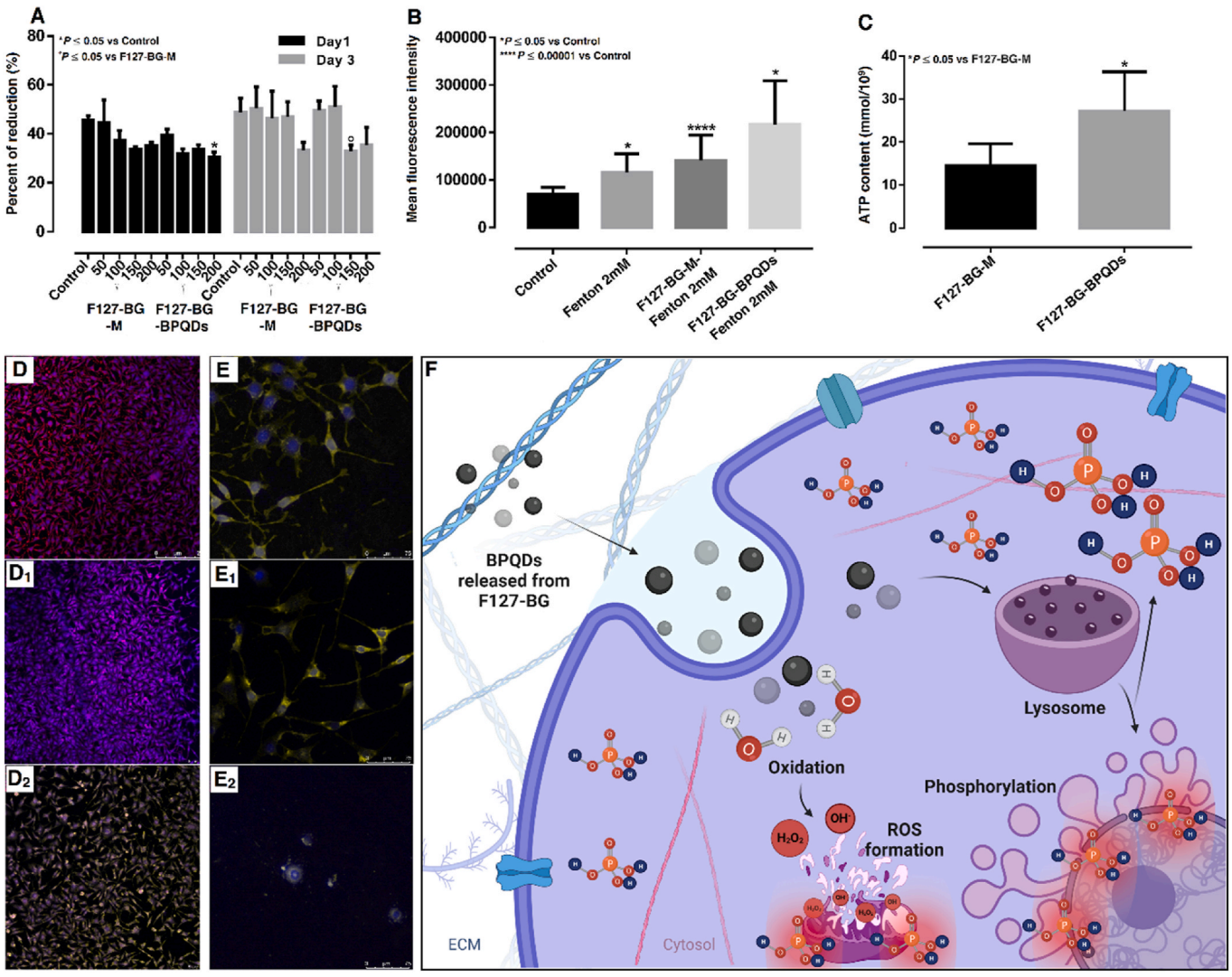

Fig. 7. Cell viability and inherent anticancer activity of the samples. (A) Cell viability of samples against SAOS-2 at various concentrations up to 72 h. **(B)** ROS generated when the samples were exposed to SAOS-2 cells after 24 h. **(C)** ATP content in SAOS-2 cells being exposed to the samples after 72 h. Caspase-3 expression was marked through the green signal of **(D)** control, **(D_1)** F127-BG-M, and **(D_2)** F127-BG-BPQDs after 72 h. Annexin V staining of **(E)** control, **(E_1)** F127-BG-M, and **(E_2)** F127-BG-BPQDs after 72 h. **(F)** An illustration of the anticancer mechanism of F127-BG-BPQDs when exposed to the cancer cells. Created with BioRender.com.

proliferation of osteoblast and differentiation of mesenchymal stem cells [15]. In 2020, another group reported a complementary study shedding light on the BP mechanism of selective anticancer activity. Different cancer cells were treated with BP in different concentrations and to prevent any potential interference no external stimulus was applied to BP during the biological studies. Based on the obtained results, BP generated higher ROS concentrations in cancer cells than the healthy ones. Higher phosphate anion concentrations led to an increase in lipid peroxidation and a reduction of superoxide dismutase, which at last results in the formation of ROS, and these species leave some irreversible damage behind to cell cytoskeleton, cell cycle, DNA followed by apoptosis [14]. Based on the obtained results, the phosphorylation and ROS generation in the cancer cells due to the degradation of BPQDs were the main reasons why the apoptosis occurred in SAOS-2 cells.

Apart from the inherent anticancer activity of BP, we also exposed the samples to NIR irradiation to increase the anticancer activity of F127-BG-BPQDs. Since the lowest concentration by which F127-BG-BPQDs showed anticancer potential was 150 μg mL^{-1}, it was chosen for NIR-applied cell viability up to 72 h. The results shown in Fig. 8(A) confirm that the composite shows inherent anticancer activity at 150 μg mL^{-1}. Moreover, applying the NIR stimulus was accompanied by an increase in the anticancer activity of the sample. During the assay, two light irradiation cycles were applied in which the cell plates were exposed to light for 20 min. The change in the temperature of each well was measured and shown in Fig. 8(B). The control (cell culture medium containing SAOS-2 cells without any material) and F127-BG-M showed a mild increase in temperature up to 40 and 42 °*C*, respectively which resulted from the light irradiation and not any light-responsive agent inside. However, F127-BG-BPQDs experienced a steeper increase in temperature, which finally reached 48 °*C* approximately. It is known that heating above 43 °*C* can induce irreversible damage to cancer cells without negative effects on the healthy cells [67]. The hyperthermia mechanism is illustrated in Fig. 8(C).

Progression and development of cancer occur by the dissemination of tumor cells from the primary tumor to the circulatory system followed by colonization in distant organs. The behavior of these cancerous cells—migration, adhesion, and invasion—is an important step in cancer spreading and metastasis; therefore, a study of these features is of crucial importance [66,68–70]. It is known that primary bone tumor accounts for less than 1 % of total diagnosed cancers, but metastasis from other organs to bone tissue is more common, known as secondary tumor. Even though most cancer types can spread to the bone, breast, and prostate

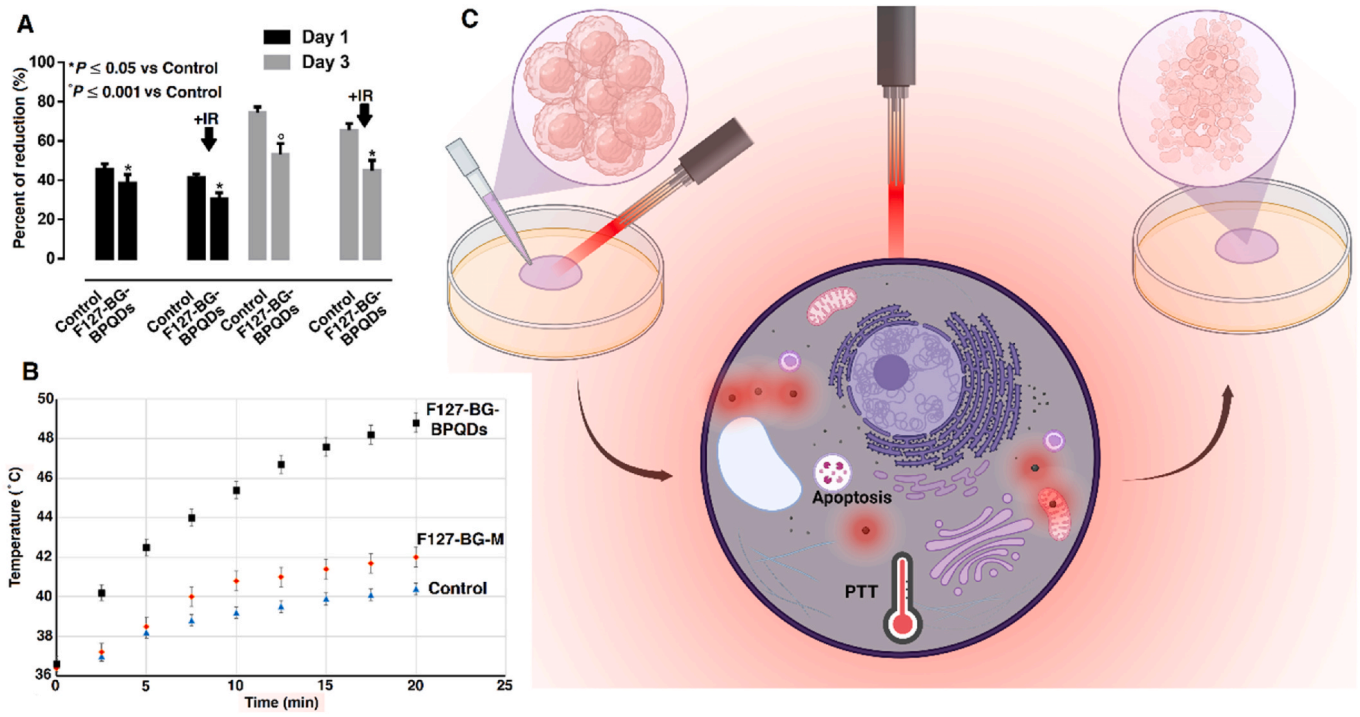

Fig. 8. Photothermal therapy potential of the samples against cancer cells. (A) Viability of SAOS-2 cells treated with F127-BG-BPQDs with and without exposure to NIR irradiation up to 72 h. **(B)** Temperature change of the culture medium. **(C)** A schematic illustration of the hyperthermia-induced anticancer potential of F127-BG-BPQDs *in vitro*. Created with BioRender.com.

cancers are more likely to affect bone tissue. These secondary tumors can cause fractures and pain in the bone tissue and also different abnormalities like hypercalcemia [71,72]. Here, we focused on a 2D migration assay (scratch assay) to assess if F127-BG-M and F127-BG-BPQDs affect the cell's migration behavior. To this aim a scratch was applied on cultured SAOS-2 and HOB cells (Fig. 9). Noteworthy, biomaterials with selective anticancer ability are supposed to prevent or decrease the migration of cancer cells, while not affecting the healthy cells' healing behavior. Nonetheless, as breast and prostate cancers are more likely to spread to the bone and form secondary tumors, we assessed the effect of BP nanomaterials on the breast cancer cells—cell viability, 2D migration, and 3D invasion—and prostate cancer cells—2D migration assay (**Figure S(4-7),** Supporting **Information**). It has already been shown in previous sections that the anticancer ability of F127-BG-BPQDs comes from the action of the encapsulated BP so we decided to test the BP nanomaterials including QDs and nanosheets on the breast and prostate cancer cells solely.

Fig. 9 indicates the exposure of F127-BG-M and F127-BG-BPQDs to the SAOS-2 and HOB cells up to 24 h; since 150 μg mL^{-1} was found as the lowest concentration of F127-BG-BPQDs inhibiting the growth of SAOS-2, this concentration was applied to both healthy and cancer cells. Four hours after applying the scratch, the images of the control plus samples were taken and the gap was clear in the middle of the plate (Fig. 9(A)). The results after 24 h revealed that the sample without BPQDs could not prevent the cancer cells' migration and the cells could fulfill the middle of the plate, whereas the BP-incorporated sample was successful in inhibiting the migration of SAOS-2 compared to the control and F127-BG-M sample (Fig. 9(C and D). In the case of HOB cells, as can be seen for the control, the migration of HOB cells was slow, but both samples stimulated the cells toward healing the scratch stemming from the biological moieties released from these samples (Fig. 9(B)). The results obtained here are in accordance with ones from the previous sections (Cell viability and inherent anticancer activity of the samples). Nonetheless, through the microwave treatment, we obtained BPQDs from the nanosheets directly and tested the cell viability and preventive effect of BPQDs against SAOS-2 as well and the results are shown in Fig. 10, where the cell viability was measured up to 72 h in the exposure of BPQDs at various concentrations—25-200 μg mL^{-1}. After the first day, an increase in the cell viability of some samples was observed while continuing the test up to 72 h was accompanied by a significant decrease in the viability of SAOS-2 from the lowest concentration. Therefore, the same concentration was chosen and applied for the scratch assay as indicated in Fig. 10(B-D). Compared to the control (SAOS-2), the BPQDs could completely prevent the cancer cells from migrating and healing the wound.

Different concentrations, from 0.5 to 25 μg mL^{-1}, of BP nanosheets and BPQDs were applied to MCF7 cells and to their normal MCF10A cells counterparts to assess cell viability at 24 h and 72 h (Fig. S4, Supporting Information). A concentration-dependent effect of BP nanomaterials was seen in MCF7 cells where concentrations from 0.5 to 5 μg mL^{-1} at 72 h reduced cell viability by nearly 50 %, and ever more than 60 % at the highest concentration. However, the cytotoxicity of BPQDs on MCF7 cells at lower concentrations of 0.5 and 1 μg mL^{-1} is higher than those induced by BP nanosheets. Notably, this effect was then reversed at higher concentrations where 5 μg mL^{-1} of BPQDs reduced MCF7 cell viability by nearly 80 % with a higher extent compared to BP nanosheets. On the other side, the cell viability results of the normal MCF10A cell counterpart showed that even the lowest concentration of BP nanosheets caused around 40 % decrease in cell viability after 72 h, and increasing concentration even reinforced this effect. Regarding the anticancer activity of BP nanomaterials against MCF-7 and SAOS-2, it can be seen that the minimum concentration required to suppress the proliferation of MCF-7 is competitively lower than that of the counterpart which can be attributed to the cell lines. The effect of BP on various cancer cell lines can change based on factors such as its biocompatibility, cellular uptake, and specific interactions with cancer cells, among other variables [15,71]. Typically, SAOS-2 and MCF-7 are frequently employed cell lines in cancer research, yet they stem from distinct cancer types and show different properties, including responsiveness to chemotherapy and aggressiveness. SAOS-2 cells are

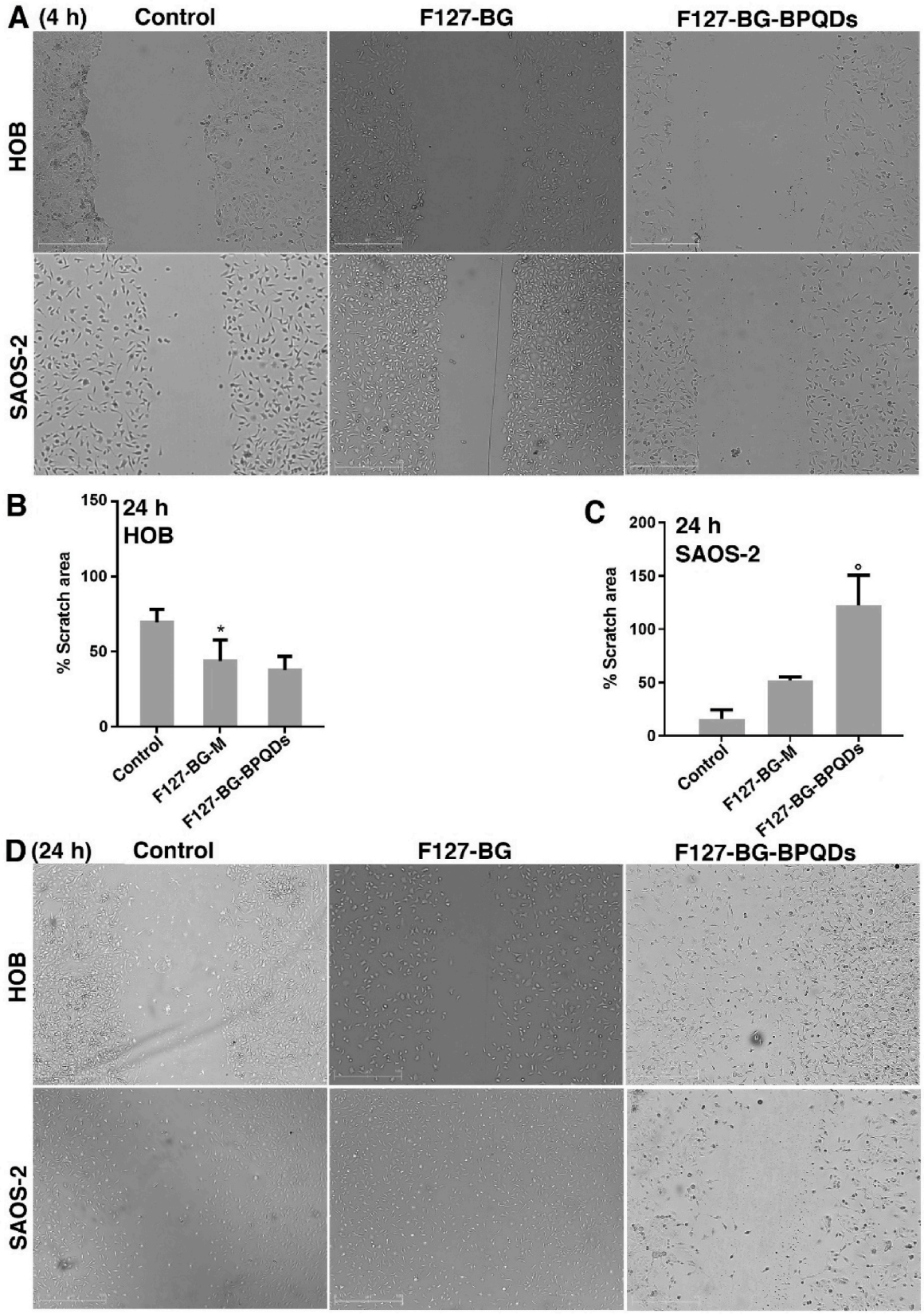

Fig. 9. 2D migration assay against healthy and cancerous bone cells *in vitro*. (A) Images were taken from the samples and control (SAOS-2 and HOB) 4 h after applying the scratch on the wells. Quantitative results related to scratch area (%) after 24 h for **(B)** HOB and **(C)** SAOS-2. $^{*}P \leq 0.05$, $^{\circ}P \leq 0.001$. **(D)** Images taken from the samples and control (SAOS-2 and HOB) 24 h after applying the scratch on the wells.

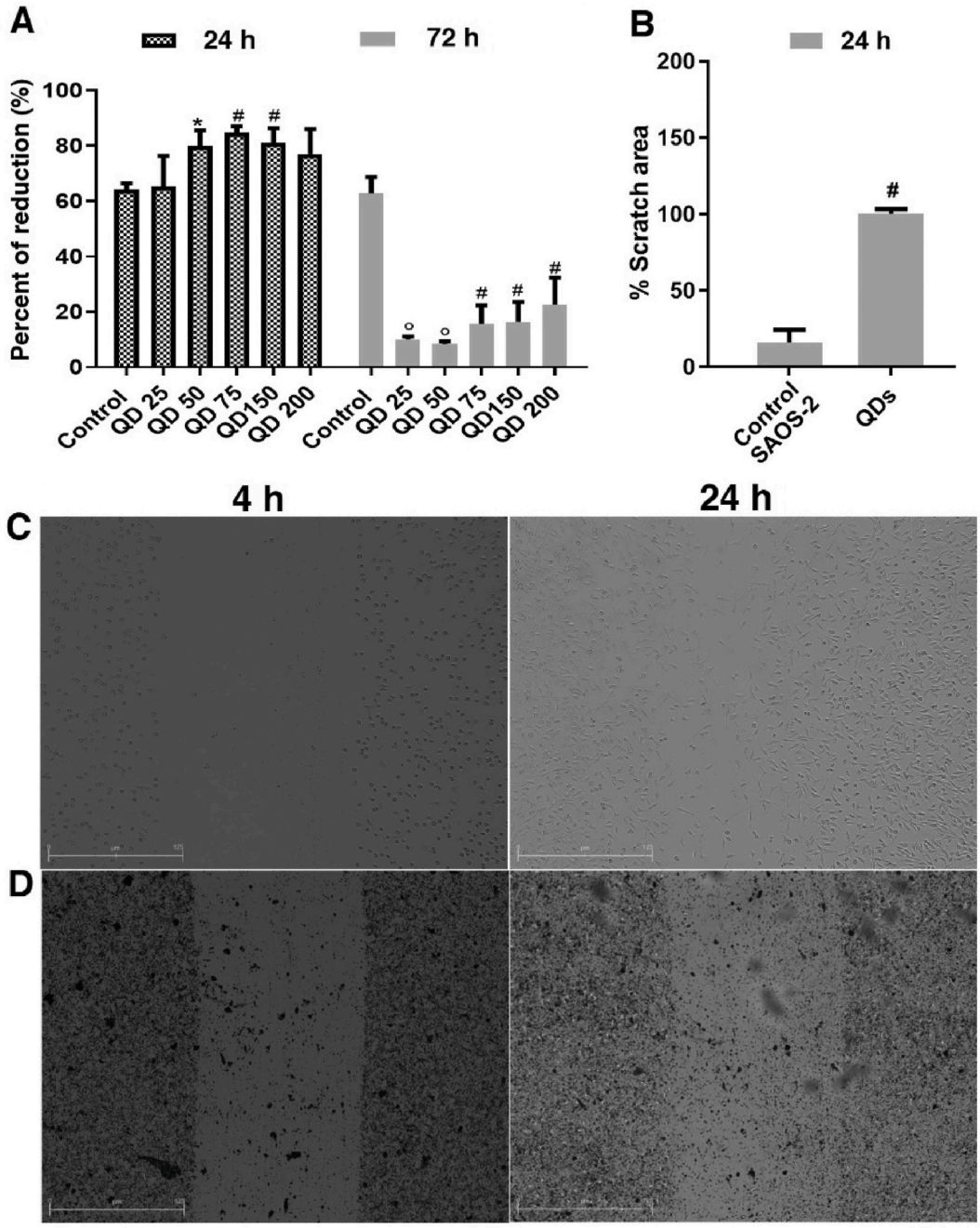

Fig. 10. Cell viability and 2D migration assay of BPQDs against SAOS-2 cells. (A) Cell viability of BPQDs at various concentrations against SAOS-2 after 24 and 72 h $^{*}P \leq 0.05$, $^{\#}P \leq 0.001$, $^{\circ}P \leq 0.0001$. **(B)** Quantitative results related to the migration assay after 24 h. Images taken from the wells after 4 and 24 h; **(C)** control (SAOS-2) and **(D)** BPQDs-treated SAOS-2 cells.

derived from human osteosarcoma, whereas MCF-7 cells originate from human breast adenocarcinoma, representing a specific subtype of breast cancer and serving as a model for hormone-responsive breast cancer [73,74]. Regarding their sensitivity to chemotherapeutic drugs, SAOS-2 cells generally exhibit lower responsiveness to conventional chemotherapy and display higher aggressiveness compared to MCF-7 cells [73,74]. Consequently, the concentration of BP utilized for SAOS-2 treatment is higher than that used for MCF-7 due to these differences. Conversely, BPQDs treatment of MCF10A cells at 0.5 and 1 μg mL^{-1} resulted in a very low cytotoxic effect. This cytotoxicity strongly increased at higher concentrations, and linearly, from 5 to 25 μg mL^{-1}. Based on this cell viability data, we decided to reduce the concentration of BP nanomaterials and evaluated their effect *in vitro* through 2D migration and 3D invasion assays in MCF7, MCF10A (the normal counterpart), and MDA-MB-231 as the most aggressive, invasive and poorly differentiated triple-negative breast cancer cell line [**Fig. S(4,5)**, Supporting **Information**]. All the cells were exposed for 24 h to 0.02, 0.05, and 0.1 μg mL^{-1} of BPQDs or BP nanosheets. As shown in Fig. S4, the BP nanosheets reduced the cell migration ability of MDA-MB-231 cells at the lowest 0.02 μg mL^{-1} concentration compared to BPQDs. However, increased concentration of BPQDs to 0.05 and 0.1 μg mL^{-1} strongly impaired MDA-MB-231 cell migration. Similar behavior was observed for MCF7 cells with the only difference that stronger BP nanomaterials effects were seen at 0.02 μg mL^{-1} and even more with a complete inhibition of cell migration at 0.05 and 0.1 μg mL^{-1}. The inhibitory effects of BP nanomaterials on the MCF10A as a healthy cell

line were weak and it is visible that all the concentrations for the nanosheets did not negatively affect cell motility. Along the same line, the cells upon BPQDs treatment could nearly fulfill the gap and reduce it as a result of the selective anticancer effect of BP nanomaterials.

To better mimic the physiological invasion conditions we analyzed the effects of BP nanosheets and BPQDs on MDA-MB-231, MCF7, and MCF10A cell movement through a 3D matrix, where cells must modify their shape and interact with the extracellular matrix (ECM *e.g.,* Matrigel) to adhere, migrate and finally invade. We used the Boyden chamber where a thin layer of Matrigel covers the porous filters positioned between the upper and bottom chambers. The cells are plated on the top of the chamber and beneath the filter there is a medium containing chemoattractants which allow the cells to migrate through the pores, to the other side of the membrane [68] [Fig. S6(A), Supporting Information]. The invasive cells able to degrade the matrix and cross the membrane pore were fixed and analyzed under microscopy after Hoechst nuclear staining. Representative images of invasive breast cancer cells treated with BPNSs and BPQDs are shown in Fig. S6(B), Supporting Information. Based on the fact that 0.1 μg mL^{-1} was the concentration able to inhibit cell migration of both breast cancer cells without affecting the normal cell counterpart (Fig. S5, Supporting Information), this concentration has been further used in the invasion assay. After 24 h of treatment, BP nanomaterials strongly impaired the invasion ability of MCF7 cells, and as expected, no effect was seen in either control MCF10A healthy cells or non-treated cells. This data indicates the biocompatible nature of BP nanomaterials at this concentration. Noteworthy, there is no significant difference between the nanosheets and BPQDs in terms of selective anticancer activity. In the case of MDA-MB-231, the cells could migrate through the filter, but the quantity was decreased to nearly half indicating the effect of both BP nanomaterials to slow down and reduce the migratory behavior of this type of cell as the most aggressive breast cancer cell line.

The effect of BPQDs and BP nanosheets at various concentrations spanning from 0.5 to 5 μg mL^{-1} on the migration behavior of prostate cancer cells (PC-3) was assessed after 24 h (Fig. S7, Supporting Information). Our group has recently performed comprehensive *in vitro* biological studies on the BP nanomaterial's selective anticancer activity against healthy (PNT-2) and cancerous (PC-3) prostate cells to understand the optimized concentration which prevents cancer cell growth with no adverse effects on the healthy ones. Different concentrations of BP nanosheets (5–75 μg mL^{-1}) were tested against both cell lines up to 72 h. It turned out that 5 μg mL^{-1} could induce nearly 40 % reduction in the cancer cells viability after 72 h and both 25 and 75 μg mL^{-1} decreased the viability down to 50 %. However, 25 and 75 μg mL^{-1} caused cytotoxicity to the healthy cells after 72 h (nearly 60 % reduction), and thus, 5 μg mL^{-1} was found as the optimized safe concentration for the healthy cells with inhibitory effects on the PC-3 cells [71]. Herein, we applied four concentrations (0.5, 1, 3, and 5 μg mL^{-1}) to assess which concentration could prevent the migration of PC-3 cells. As can be seen in Fig. S7, the lower concentrations (0.5 and 1 μg mL^{-1}) failed to make inhibitory effects on the cancer cells, whereas 3 μg mL^{-1} and even more 5 μg mL^{-1} were strong enough to prevent the cancer cells from healing the wound. Nonetheless, there was no significant difference in anti-migratory effect noticed between the BP nanomaterials. Therefore, it can be concluded that 3 μg mL^{-1} was the lowest effective concentration affecting PC-3 cell migration *in vitro* and this concentration was much lower for breast cancer cells indicating the higher susceptibility of breast cancer cells towards BP nanomaterials than prostate and bone cancer cells.

One of the main aims of the present study was to come up with a therapeutic agent capable of impeding cancer cell growth, but we also aimed at a regenerative effect of the same because having a multifunctional platform able to induce effective therapeutic approaches followed by defect repair is of great value. Therefore, the regeneration potential of F127-BG-M and F127-BG-BPQDs was tested against healthy osteoblast cells up to 72 h (Fig. 11(A)). Compared to the control, F127-BG-M shows a significant increase in cell viability, which can be attributed to the release of stimulating ions from this sample, including Ca^{2+}, SiO_4^{4-}, and PO_4^{3-}, all of which could trigger the osteoblast's proliferation and growth. Moreover, F127-BG-BPQDs show a higher cell viability improvement than the counterpart without BPQDs; this difference can be attributed to the action of BPQDs. As mentioned before, BP undergoes degradation in biological media, producing PO_4^{3-} ions that trigger cell proliferation [12]. The cell viability and osteogenic differentiation (ALP, OPN, and OCN expression) of human mesenchymal stem cells in the presence of F127-BG-M and F127-BG-BPQDs were examined for up to 14 days *in vitro* (Fig. 11(B-D)). The cell viability results showed that the samples did not affect negatively the cells, with data being very close to those of the control. The ALP activity, an early marker of osteogenesis, was also assessed to confirm if the composites could induce osteogenic differentiation of the stem cells (Fig. 11(C)). F127-BG-BPQDs showed significantly higher ALP activity on the 7th and 14th days than that of the counterpart without BP which followed the same trend as the control. Moreover, the OPN expression as a highly phosphorylated sialoprotein and a main part of the mineralized extracellular matrices of bones was assessed after 14 days. As shown in Fig. 11(D), F127-BG-BPQDs was found to induce OPN expression (red signal) in human mesenchymal stem cells after 14 days of cell culture without osteogenic supplements in cell culture media, whereas the same signal was not visible for the sample without BP. Nonetheless, analogous results were also observed for OCN assay. OCN is a key player throughout the endocrinology of bone and osteoblasts can only express and secrete this protein factor. It is known that collagen type I and Runx2 are expressed as the direct result of OCN's expression and OCN is an important calcium-binding protein leading to the development of bone extracellular matrix and a sign of terminal differentiation; at this stage, osteoblasts generate calcified tissue [75]. The OCN expression was assessed for F127-BG-M and F127-BG-BPQDs samples after 14 days (Fig. 11(E)) and the red signals observed for the F127-BG-BPQDs were related to OCN expression. The results suggest that the presence of BP speeds up both OPN and OCN expressions compared to the effect of other bioglasses mentioned in the literature that were able to induce OPN expression only after 21 days of cell culture in basal conditions [76]. Previous studies reported that BP has the potential to promote either osteoblast or mesenchymal stem cells' osteogenesis [20,77,78]. This osteogenic property has been ascribed to both the physical structure and the by-products released after the degradation of BP up to a definite concentration. The structure provides mechanical cues for the stem cells leading to a desirable environment for the differentiation of these cells. Nonetheless, it is known that BP's degradation brings to the release of phosphate ions that have a pivotal role in the mineralization of extracellular matrix and trabeculae formation [79,80]. The results obtained in this section show that the F127-BG-BPQDs can stimulate the osteoblast cells towards proliferation and also induce the osteogenic differentiation of hMSCs.

4. Conclusions

A theragenerative (therapeutic + regenerative) platform was designed and realized through a two-step synthesis strategy—evaporation-induced self-assembly and microwave treatment. The addition of Pluronic F127 and microwave treatment were found to improve the physicochemical and cell compatibility (against fibroblast cells) properties of samples; the polymer could distribute all the ions homogeneously over the surface whereas in the absence of Pluronic F127, inhomogeneous ion distribution had been yielded. The microwave treatment did not affect the ions distribution, but improved the chemical stability through forming some crystalline phases throughout the BG structure. In the case of BP-incorporated composites, the microwave treatment successfully turned the BPNSs into BPQDs *in situ* which were homogenously distributed throughout the composite. The *in vitro* bioactivity and degradation assays of samples revealed that BP, either in

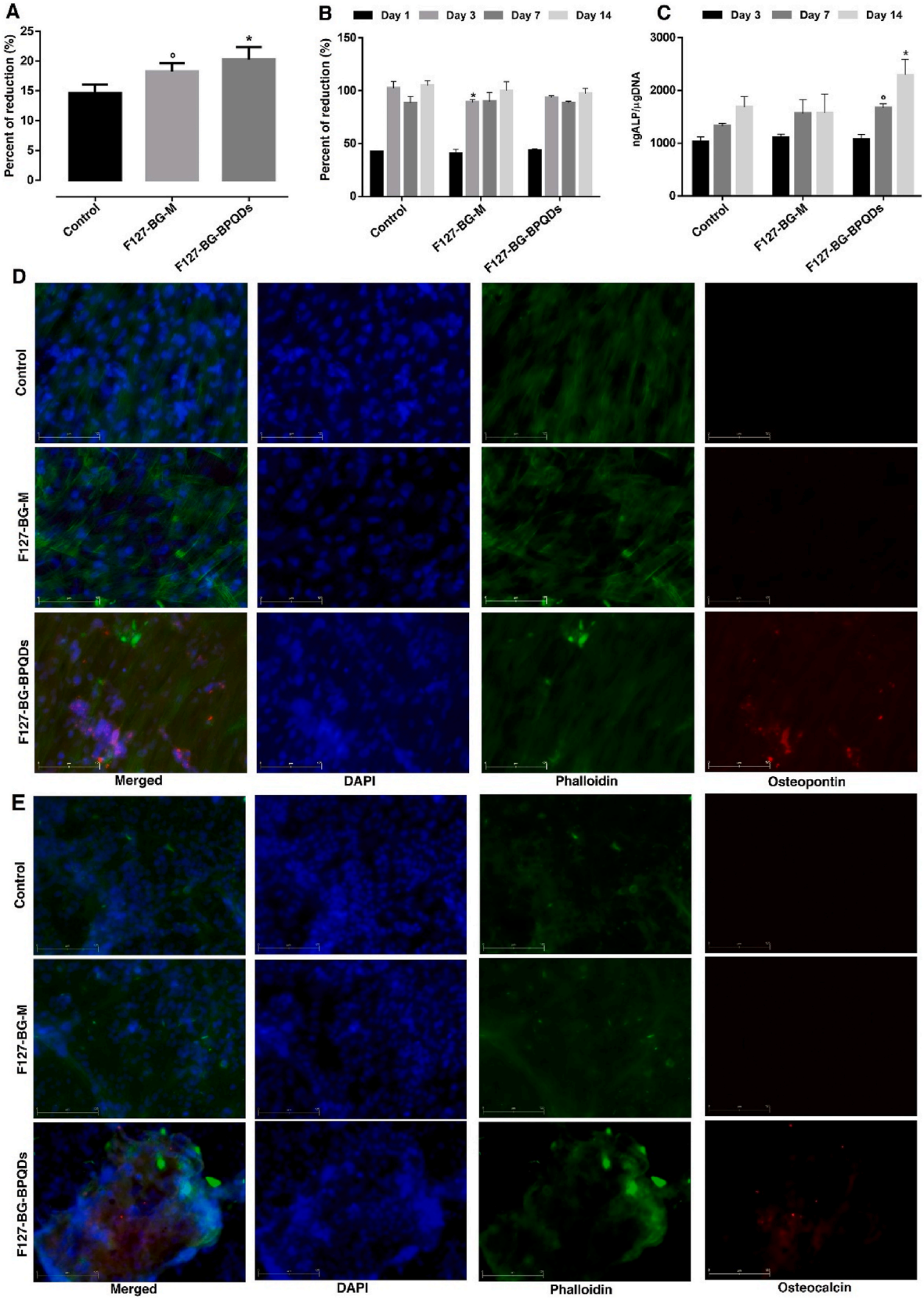

Fig. 11. Regenerative potential of the samples *in vitro*. Cell viability of samples against **(A)** healthy osteoblast cells after 72 h and **(B)** human mesenchymal stem cells up to 14 days. **(C)** ALP activity of samples in the presence of mesenchymal stem cells. **(D)** Images taken after 14 days; OPN expression is shown in red. **(E)** Images taken after 14 days; OCN expression is shown in red. $^{*}P \leq 0.05$ vs F127-BG-M and $^{\circ}P \leq 0.001$ vs control.

the form of nanosheets or quantum dots, made a significant improvement in bioactivity and chemical stability. Moreover, the encapsulation of BPQDs in the composite could considerably decrease their oxidation degree. The anticancer potential of F127-BG-M and F127-BG-BPQDs samples was tested against osteosarcoma cells up to 72 h and the sample with BPQDs induced a significant decrease in the proliferation rate at 150 μg mL^{-1} whereas the one without BPQDs at the same concentration significantly improved cell viability compared to the control. An anticancer mechanism was proposed and the potential pathways were assessed. The anticancer activity was related to the ROS generated as the result of BPQDs degradation. To improve the anticancer efficacy further, NIR irradiation was also applied *in vitro* and resulted in a greater increase in cell growth suppression as the result of hyperthermia. The effect of BP nanomaterials (nanosheets and quantum dots) and the corresponding composites on the migration and invasion of different cancer cell lines was assessed *in vitro*; it turned out that the BP-incorporated composite could prevent migration of SAOS-2 cells and the BP nanomaterials induced inhibitory effects on the breast and prostate cancer cells as they are more likely to metastasize to bone tissue. The regenerative potential of both samples—F127-BG-M and F127-BG-BPQDs—was evaluated in the exposure of healthy osteoblast and human mesenchymal stem cells. The one with BPQDs outperformed the others stimulated the cells toward proliferation and induced the stem cells toward osteogenic differentiation. The overall results implied that the F127-BG-BPQDs nanocomposite developed in this study is a promising theragenerative platform for bone cancer since it was proven to simultaneously induce an effective therapeutic approach to primary and secondary bone cancers and bone tissue regeneration.

Ethics approval and consent to participate

The study does not include:

- Clinical study
- Experimentation on animals
- Human subjects

Availability of data and materials

The datasets during and/or analyzed during the current study available from the corresponding author on reasonable request.

CRediT authorship contribution statement

Ashkan Bigham: Writing – original draft, Validation, Software, Methodology, Investigation, Data curation, Conceptualization. **Ines Fasolino:** Methodology, Investigation. **Silvia Borsacchi:** Writing – review & editing, Methodology, Investigation, Formal analysis. **Carmen Valente:** Writing – review & editing, Methodology, Investigation. **Lucia Calucci:** Methodology. **Gabriele Turacchio:** Methodology, Investigation. **Marianna Pannico:** Methodology, Investigation. **Manuel Serrano-Ruiz:** Methodology, Investigation, Formal analysis. **Luigi Ambrosio:** Writing – review & editing, Supervision, Resources. **Maria Grazia Raucci:** Writing – review & editing, Supervision, Resources, Project administration, Funding acquisition, Data curation, Conceptualization.

Declaration of competing interest

The authors have declared that there is no conflict of interest.

Acknowledgement

The authors acknowledge support from Progetto MIUR PRIN2017–ACTION, Grant No. 2017SZ5WZB and POR Campania FESR 2014–2020 (Campania imaging Infrastructure for Research in Oncology – C.I.R.O). The authors also thank Maria Rosaria Bonetti for lab technical support, Cristina Del Barone for facilitating microscopy analysis, Dr. Antonio Pennetta for ICP analysis and Dr. Roberta Marzella for support to project management. CISUP (Centre for Instrument Sharing-University of Pisa) and the EUroBioImaging (EUBI) Facility at CNR (Naples) are acknowledged for the use of the Bruker Avance NEO 500 Solid State NMR spectrometer and of AxioVision microscope (Carl Zeiss Micro Imaging GmbH), respectively.

Appendix A. Supplementary data

Supplementary data to this article can be found online at https://doi.org/10.1016/j.bioactmat.2024.01.018.

References

[1] L. Li, J. Eyckmans, C.S. Chen, Designer biomaterials for mechanobiology, Nat. Mater. 16 (2017) 1164–1168, https://doi.org/10.1038/nmat5049.
[2] P. Zhang, Y. Li, W. Tang, J. Zhao, L. Jing, K.J. McHugh, Theranostic nanoparticles with disease-specific administration strategies, Nano Today 42 (2022) 101335, https://doi.org/10.1016/j.nantod.2021.101335.
[3] A. Bigham, M.G. Raucci, K. Zheng, A.R. Boccaccini, L. Ambrosio, Oxygen-deficient bioceramics: combination of diagnosis, therapy, and regeneration, Adv. Mater. n/a (2023) 2302858, https://doi.org/10.1002/adma.202302858.
[4] B. Chen, H. Xiang, S. Pan, L. Yu, T. Xu, Y. Chen, B. Chen, H. Xiang, S. Pan, L. Yu, Y. Chen, T. Xu, Advanced theragenerative biomaterials with therapeutic and regeneration Multifunctionality, Adv. Funct. Mater. 30 (2020) 2002621, https://doi.org/10.1002/ADFM.202002621.
[5] X. Xu, X. Chen, H. Wang, X. Mei, B. Chen, R. Li, Y. Qin, Balancing the toxicity, photothermal effect, and promotion of osteogenesis: photothermal scaffolds for malignant bone tumor therapy, Mater. Today Adv. 13 (2022) 100209, https://doi.org/10.1016/j.mtadv.2022.100209.
[6] E. Sharifi, A. Bigham, S. Yousefiasl, M. Trovato, M. Ghomi, Y. Esmaeili, P. Samadi, A. Zarrabi, M. Ashrafizadeh, S. Sharifi, R. Sartorius, F. Dabbagh Moghaddam, A. Maleki, H. Song, T. Agarwal, T.K. Maiti, N. Nikfarjam, C. Burvill, V. Mattoli, M. G. Raucci, K. Zheng, A.R. Boccaccini, L. Ambrosio, P. Makvandi, Mesoporous bioactive glasses in cancer diagnosis and therapy: stimuli-responsive, toxicity, Immunogenicity, and clinical translation, Adv. Sci. n/a (2021) 2102678, https://doi.org/10.1002/advs.202102678.
[7] Y. Liu, J. Ding, Q. Wang, M. Wen, T. Tang, Y. Liu, R. Yuan, Y. Li, M. An, Research progress on the biomedical uses of graphene and its derivatives, New Carbon Mater 36 (2021) 779–793, https://doi.org/10.1016/S1872-5805(21)60073-2.
[8] A. Maleki, M. Ghomi, N. Nikfarjam, M. Akbari, E. Sharifi, M.-A. Shahbazi, M. Kermanian, M. Seyedhamzeh, E. Nazarzadeh Zare, M. Mehrali, O. Moradi, F. Sefat, V. Mattoli, P. Makvandi, Y. Chen, Biomedical applications of MXene-integrated composites: regenerative medicine, infection therapy, cancer treatment, and biosensing, Adv. Funct. Mater. 32 (2022) 2203430, https://doi.org/10.1002/adfm.202203430.
[9] Z. Tu, G. Guday, M. Adeli, R. Haag, Multivalent interactions between 2D nanomaterials and biointerfaces, Adv. Mater. 30 (2018) 1–27, https://doi.org/10.1002/adma.201706709.
[10] K. Hu, L. Xie, Y. Zhang, M. Hanyu, Z. Yang, K. Nagatsu, H. Suzuki, J. Ouyang, X. Ji, J. Wei, H. Xu, O.C. Farokhzad, S.H. Liang, L. Wang, W. Tao, M.-R. Zhang, Marriage of black phosphorus and Cu2+ as effective photothermal agents for PET-guided combination cancer therapy, Nat. Commun. 11 (2020) 2778, https://doi.org/10.1038/s41467-020-16513-0.
[11] A. Bigham, V. Rahimkhoei, P. Abasian, M. Delfi, J. Naderi, M. Ghomi, F. Dabbagh Moghaddam, T. Waqar, Y. Nuri Ertas, S. Sharifi, N. Rabiee, S. Ersoy, A. Maleki, E. Nazarzadeh Zare, E. Sharifi, E. Jabbari, P. Makvandi, A. Akbari, Advances in tannic acid-incorporated biomaterials: infection treatment, regenerative medicine, cancer therapy, and biosensing, Chem. Eng. J. (2021) 134146, https://doi.org/10.1016/j.cej.2021.134146.
[12] B. Yang, J. Yin, Y. Chen, S. Pan, H. Yao, Y. Gao, J. Shi, 2D-Black-Phosphorus-Reinforced 3D-printed scaffolds:A stepwise countermeasure for osteosarcoma, Adv. Mater. 30 (2018) 1705611, https://doi.org/10.1002/ADMA.201705611.
[13] W. Zhou, T. Pan, H. Cui, Z. Zhao, P.K. Chu, X.F. Yu, Black phosphorus: bioactive nanomaterials with inherent and selective chemotherapeutic effects, Angew. Chemie Int. Ed. 58 (2019) 769–774, https://doi.org/10.1002/ANIE.201810878.
[14] N. Kong, X. Ji, J. Wang, X. Sun, G. Chen, T. Fan, W. Liang, H. Zhang, A. Xie, O. C. Farokhzad, W. Tao, Ros-mediated selective killing effect of black phosphorus: mechanistic understanding and its guidance for safe biomedical applications, Nano Lett. 20 (2020) 3943–3955, https://doi.org/10.1021/ACS.NANOLETT.0C01098/ASSET/IMAGES/LARGE/NL0C01098_0007.JPEG.
[15] M.G. Raucci, I. Fasolino, M. Caporali, M. Serrano-Ruiz, A. Soriente, M. Peruzzini, L. Ambrosio, Exfoliated black phosphorus promotes in vitro bone regeneration and suppresses osteosarcoma progression through cancer-related inflammation inhibition, ACS Appl. Mater. Interfaces 11 (2019) 9333–9342, https://doi.org/10.1021/ACSAMI.8B21592/ASSET/IMAGES/LARGE/AM-2018-21592M_0009.JPEG.
[16] V. Mussi, I. Fasolino, D. Paria, S. De Simone, M. Caporali, M. Serrano-Ruiz, L. Ambrosio, I. Barman, M.G. Raucci, A. Convertino, Label-free morpho-molecular

imaging for studying the differential interaction of black phosphorus with tumor cells, Nanomaterials 12 (2022), https://doi.org/10.3390/nano12121994.
[17] Y. Zhang, C. Ma, J. Xie, H. Ågren, H. Zhang, Black phosphorus/polymers: status and challenges, Adv. Mater. 33 (2021) 2100113, https://doi.org/10.1002/adma.202100113.
[18] X. Liu, M.N. George, L. Li, D. Gamble, A.L. Miller, B. Gaihre, B.E. Waletzki, L. Lu, Injectable electrical conductive and phosphate releasing gel with two-dimensional black phosphorus and carbon nanotubes for bone tissue engineering, ACS Biomater. Sci. Eng. 6 (2020) 4653–4665, https://doi.org/10.1021/ACSBIOMATERIALS.0C00612/ASSET/IMAGES/LARGE/AB0C00612_0007.JPEG.
[19] G. Zeng, Y. Chen, Surface modification of black phosphorus-based nanomaterials in biomedical applications: strategies and recent advances, Acta Biomater. 118 (2020) 1–17, https://doi.org/10.1016/j.actbio.2020.10.004.
[20] X. Liu, A.L. Miller, S. Park, M.N. George, B.E. Waletzki, H. Xu, A. Terzic, L. Lu, Two-dimensional black phosphorus and graphene oxide nanosheets synergistically enhance cell proliferation and osteogenesis on 3D printed scaffolds, ACS Appl. Mater. Interfaces 11 (2019) 23558–23572, https://doi.org/10.1021/ACSAMI.9B04121/SUPPL_FILE/AM9B04121_SI_001.PDF.
[21] Z. Wang, J. Zhao, W. Tang, L. Hu, X. Chen, Y. Su, C. Zou, J. Wang, W.W. Lu, W. Zhen, R. Zhang, D. Yang, S. Peng, Multifunctional nanoengineered hydrogels consisting of black phosphorus nanosheets upregulate bone formation, Small 15 (2019) 1901560, https://doi.org/10.1002/SMLL.201901560.
[22] C. Xing, S. Chen, M. Qiu, X. Liang, Q. Liu, Q. Zou, Z. Li, Z. Xie, D. Wang, B. Dong, L. Liu, D. Fan, H. Zhang, Conceptually novel black phosphorus/cellulose hydrogels as promising photothermal agents for effective cancer therapy, Adv. Healthcare Mater. 7 (2018) 1701510, https://doi.org/10.1002/adhm.201701510.
[23] L. Zhou, N. Liu, L. Feng, M. Zhao, P. Wu, Y. Chai, J. Liu, P. Zhu, R. Guo, Multifunctional electrospun asymmetric wettable membrane containing black phosphorus/Rg1 for enhancing infected wound healing, Bioeng. Transl. Med. 7 (2022) e10274, https://doi.org/10.1002/btm2.10274.
[24] L. Cheng, Z. Chen, Z. Cai, J. Zhao, M. Lu, J. Liang, F. Wang, J. Qi, W. Cui, L. Deng, Bioinspired functional black phosphorus electrospun fibers achieving recruitment and biomineralization for staged bone regeneration, Small 16 (2020) 2005433, https://doi.org/10.1002/smll.202005433.
[25] S. Li, Y. Qing, Y. Lou, R. Li, H. Wang, X. Wang, B. Ying, X. Tang, Y. Qin, Injectable thermosensitive black phosphorus nanosheet- and doxorubicin-loaded hydrogel for synergistic bone tumor photothermal-chemotherapy and osteogenesis enhancement, Int. J. Biol. Macromol. 239 (2023) 124209, https://doi.org/10.1016/J.IJBIOMAC.2023.124209.
[26] Y. Zhao, X. Peng, X. Xu, M. Wu, F. Sun, Q. Xin, H. Zhang, L. Zuo, Y. Cao, Y. Xia, J. Luo, C. Ding, J. Li, Chitosan based photothermal scaffold fighting against bone tumor-related complications: recurrence, infection, and defects, Carbohydr. Polym. 300 (2023) 120264, https://doi.org/10.1016/J.CARBPOL.2022.120264.
[27] K. Du, W. Yang, S. Deng, X. Li, P. Yang, High-quality black phosphorus quantum dots fabricated via microwave-tailored technology, Nanomaterials 10 (2020), https://doi.org/10.3390/nano10010139.
[28] T. Kokubo, H. Takadama, How useful is SBF in predicting in vivo bone bioactivity? Biomaterials 27 (2006) 2907–2915, https://doi.org/10.1016/j.biomaterials.2006.01.017.
[29] M. V Zamaraeva, R.Z. Sabirov, E. Maeno, Y. Ando-Akatsuka, S. V Bessonova, Y. Okada, Cells die with increased cytosolic ATP during apoptosis: a bioluminescence study with intracellular luciferase, Cell Death Differ. 12 (2005) 1390–1397, https://doi.org/10.1038/sj.cdd.4401661.
[30] A. Bigham, S.A. Hassanzadeh-Tabrizi, M. Rafienia, H. Salehi, Ordered mesoporous magnesium silicate with uniform nanochannels as a drug delivery system: the effect of calcination temperature on drug delivery rate, Ceram. Int. (2016), https://doi.org/10.1016/j.ceramint.2016.08.009.
[31] N. Khamsehashari, S.A. Hassanzadeh-Tabrizi, A. Bigham, Effects of strontium adding on the drug delivery behavior of silica nanoparticles synthesized by P123-assisted sol-gel method, Mater. Chem. Phys. 205 (2018) 283–291, https://doi.org/10.1016/j.matchemphys.2017.11.034.
[32] M. Agafonov, T. Volkova, R. Kumeev, E. Chibunova, I. Terekhova, Impact of pluronic F127 on aqueous solubility and membrane permeability of antirheumatic compounds of different structure and polarity, J. Mol. Liq. 274 (2019) 770–777, https://doi.org/10.1016/j.molliq.2018.11.060.
[33] Y.-J. Zhu, F. Chen, Microwave-assisted preparation of inorganic nanostructures in liquid phase, Chem. Rev. 114 (2014) 6462–6555, https://doi.org/10.1021/cr400366s.
[34] C. Migneco, E. Fiume, E. Verné, F. Baino, A guided walk through the world of mesoporous bioactive glasses (MBGs): fundamentals, processing, and applications, Nanomaterials 10 (2020), https://doi.org/10.3390/nano10122571.
[35] I. Izquierdo-Barba, M. Colilla, M. Manzano, M. Vallet-Regí, In vitro stability of SBA-15 under physiological conditions, Microporous Mesoporous Mater. 132 (2010) 442–452, https://doi.org/10.1016/j.micromeso.2010.03.025.
[36] S.A. Hassanzadeh-Tabrizi, A. Bigham, M. Rafienia, Surfactant-assisted sol-gel synthesis of forsterite nanoparticles as a novel drug delivery system, Mater. Sci. Eng. C. 58 (2016), https://doi.org/10.1016/j.msec.2015.09.020.
[37] M. Schumacher, P. Habibovic, S. van Rijt, Mesoporous bioactive glass composition effects on degradation and bioactivity, Bioact. Mater. 6 (2021) 1921–1931, https://doi.org/10.1016/j.bioactmat.2020.12.007.
[38] A. López-Noriega, D. Arcos, I. Izquierdo-Barba, Y. Sakamoto, O. Terasaki, M. Vallet-Regí, Ordered mesoporous bioactive glasses for bone tissue regeneration, Chem. Mater. 18 (2006) 3137–3144, https://doi.org/10.1021/cm060488o.
[39] B. Yu, C.A. Turdean-Ionescu, R.A. Martin, R.J. Newport, J. V Hanna, M.E. Smith, J. R. Jones, Effect of calcium source on structure and properties of sol–gel derived bioactive glasses, Langmuir 28 (2012) 17465–17476, https://doi.org/10.1021/la303768b.
[40] G. Poologasundarampillai, B. Yu, J.R. Jones, T. Kasuga, Electrospun silica/PLLA hybrid materials for skeletal regeneration, Soft Matter 7 (2011) 10241–10251, https://doi.org/10.1039/C1SM06171B.
[41] N. Cao, X.B. Chen, D.J. Schreyer, Influence of calcium ions on cell survival and proliferation in the context of an alginate hydrogel, ISRN Chem. Eng. 2012 (2012) 516461, https://doi.org/10.5402/2012/516461.
[42] N. Aslankoohi, K. Mequanint, Poly(ester amide)–bioactive glass hybrid biomaterials for bone regeneration and biomolecule delivery, ACS Appl. Bio Mater. 3 (2020) 3621–3630, https://doi.org/10.1021/acsabm.0c00257.
[43] C. Bossard, H. Granel, É. Jallot, V. Montouillout, F. Fayon, J. Soulié, C. Drouet, Y. Wittrant, J. Lao, Mechanism of calcium incorporation inside sol–gel silicate bioactive glass and the advantage of using Ca(OH)2 over other calcium sources, ACS Biomater. Sci. Eng. 5 (2019) 5906–5915, https://doi.org/10.1021/acsbiomaterials.9b01245.
[44] D.-S. Kuzmenka ClaudiaAU - König, AndreasAU - Flath, TobiasAU - Hahnel, Fritz P. AU - Hacker SebastianAU - Schulze, Michael C. Au - Schulz-Siegmund, MichaelaTI - sustained calcium(II)-Release to impart bioactivity in hybrid glass scaffolds for bone tissu, No title, Pharmaceutics 12 (2020), https://doi.org/10.3390/pharmaceutics12121192.
[45] J. Ouyang, R.-Y. Liu, W. Chen, Z. Liu, Q. Xu, K. Zeng, L. Deng, L. Shen, Y.-N. Liu, A black phosphorus based synergistic antibacterial platform against drug resistant bacteria, J. Mater. Chem. B 6 (2018) 6302–6310, https://doi.org/10.1039/C8TB01669K.
[46] Y. Wang, X. Hu, L. Zhang, C. Zhu, J. Wang, Y. Li, Y. Wang, C. Wang, Y. Zhang, Q. Yuan, Bioinspired extracellular vesicles embedded with black phosphorus for molecular recognition-guided biomineralization, Nat. Commun. 101 (2019) 1–10, https://doi.org/10.1038/s41467-019-10761-5, 10 (2019).
[47] W. Tao, X. Zhu, X. Yu, X. Zeng, Q. Xiao, X. Zhang, X. Ji, X. Wang, J. Shi, H. Zhang, L. Mei, Black phosphorus nanosheets as a robust delivery platform for cancer theranostics, Adv. Mater. 29 (2017) 1603276, https://doi.org/10.1002/adma.201603276.
[48] C. Sun, L. Wen, J. Zeng, Y. Wang, Q. Sun, L. Deng, C. Zhao, Z. Li, One-pot solventless preparation of PEGylated black phosphorus nanoparticles for photoacoustic imaging and photothermal therapy of cancer, Biomaterials 91 (2016) 81–89, https://doi.org/10.1016/j.biomaterials.2016.03.022.
[49] L. Qin, G. Ling, F. Peng, F. Zhang, S. Jiang, H. He, D. Yang, P. Zhang, Black phosphorus nanosheets and gemcitabine encapsulated thermo-sensitive hydrogel for synergistic photothermal-chemotherapy, J. Colloid Interface Sci. 556 (2019) 232–238, https://doi.org/10.1016/j.jcis.2019.08.058.
[50] F. Martini, S. Borsacchi, G. Barcaro, M. Caporali, M. Vanni, M. Serrano-Ruiz, M. Geppi, M. Peruzzini, L. Calucci, Phosphorene and black phosphorus: the 31P NMR view, J. Phys. Chem. Lett. 10 (2019) 5122–5127, https://doi.org/10.1021/acs.jpclett.9b01788.
[51] H. suk Yun, S. eon Kim, Y. teak Hyeon, Highly ordered mesoporous bioactive glasses with Im3m symmetry, Mater. Lett. 61 (2007) 4569–4572, https://doi.org/10.1016/J.MATLET.2007.02.075.
[52] L. Ji, Y. Si, H. Liu, X. Song, W. Zhu, A. Zhu, Application of orthogonal experimental design in synthesis of mesoporous bioactive glass, Microporous Mesoporous Mater. 184 (2014) 122–126, https://doi.org/10.1016/J.MICROMESO.2013.10.007.
[53] J.R. Brent, N. Savjani, E.A. Lewis, S.J. Haigh, D.J. Lewis, P. O'Brien, Production of few-layer phosphorene by liquid exfoliation of black phosphorus, Chem. Commun. 50 (2014) 13338–13341, https://doi.org/10.1039/C4CC05752J.
[54] A. Bigham, A.H. Aghajanian, M. Movahedi, M. Sattary, M. Rafienia, L. Tayebi, A 3D nanostructured calcium-aluminum-silicate scaffold with hierarchical meso-macroporosity for bone tissue regeneration: fabrication, sintering behavior, surface modification and in vitro studies, J. Eur. Ceram. Soc. (2020), https://doi.org/10.1016/j.jeurceramsoc.2020.07.073.
[55] A. Bigham, A.O.M. Salehi, M. Rafienia, M.R. Salamat, S. Rahmati, M.G. Raucci, L. Ambrosio, Zn-substituted Mg2SiO4 nanoparticles-incorporated PCL-silk fibroin composite scaffold: a multifunctional platform towards bone tissue regeneration, Mater. Sci. Eng. C. 127 (2021) 112242, https://doi.org/10.1016/j.msec.2021.112242.
[56] M. Rafienia, A. Bigham, A. Saudi, S. Rahmati, Gehlenite nanobioceramic: sol-gel synthesis, characterization, and in vitro assessment of its bioactivity, Mater. Lett. 225 (2018) 89–92, https://doi.org/10.1016/j.matlet.2018.04.094.
[57] A. Bigham, A.H. Aghajanian, A. Saudi, M. Rafienia, Hierarchical porous Mg_2SiO_4-$CoFe_2O_4$ nanomagnetic scaffold for bone cancer therapy and regeneration: surface modification and in vitro studies, Mater. Sci. Eng. C. 109 (2020), https://doi.org/10.1016/j.msec.2019.110579.
[58] J. Shao, C. Ruan, H. Xie, Z. Li, H. Wang, P.K. Chu, X.-F. Yu, J. Shao, C. Ruan, H. Xie, Z. Li, H. Wang, X. Yu, P.K. Chu, Black-phosphorus-incorporated hydrogel as a sprayable and biodegradable photothermal platform for postsurgical treatment of cancer, Adv. Sci. 5 (2018) 1700848, https://doi.org/10.1002/ADVS.201700848.
[59] F. Foroughi, S.A. Hassanzadeh-Tabrizi, A. Bigham, In situ microemulsion synthesis of hydroxyapatite-$MgFe_2O_4$ nanocomposite as a magnetic drug delivery system, Mater. Sci. Eng. C. 68 (2016), https://doi.org/10.1016/j.msec.2016.07.028.
[60] R.A. Youness, M.A. Taha, M. Ibrahim, A. El-Kheshen, FTIR spectral characterization, mechanical properties and antimicrobial properties of La-doped phosphate-based bioactive glasses, Silicon 10 (2018) 1151–1159, https://doi.org/10.1007/s12633-017-9587-0.
[61] N. Rocton, H. Oudadesse, B. Lefeuvre, H. Peisker, K. Rbii, Fine analysis of interaction mechanism of bioactive glass surface after soaking in SBF solution: AFM and ICP-OES investigations, Appl. Surf. Sci. 505 (2020) 144076, https://doi.org/10.1016/j.apsusc.2019.144076.

[62] Y. Rezaei, F. Moztarzadeh, S. Shahabi, M. Tahriri, Synthesis, characterization, and in vitro bioactivity of sol-gel-derived SiO2–CaO–P2O5–MgO-SrO bioactive glass, synth. React. Inorganic, met, Nano-Metal Chem. 44 (2014) 692–701, https://doi.org/10.1080/15533174.2013.783869.

[63] T. Suchý, M. Bartoš, R. Sedláček, M. Šupová, M. Žaloudková, G.S. Martynková, R. Foltán, Various simulated body fluids lead to significant differences in collagen tissue engineering scaffolds, Materials 14 (2021), https://doi.org/10.3390/ma14164388.

[64] L. Wu, J. Wang, J. Lu, D. Liu, N. Yang, H. Huang, P.K. Chu, X.-F. Yu, Lanthanide-coordinated black phosphorus, Small 14 (2018) 1801405, https://doi.org/10.1002/smll.201801405.

[65] X. Zhu, T. Zhang, D. Jiang, H. Duan, Z. Sun, M. Zhang, H. Jin, R. Guan, Y. Liu, M. Chen, H. Ji, P. Du, W. Yan, S. Wei, Y. Lu, S. Yang, Stabilizing black phosphorus nanosheets via edge-selective bonding of sacrificial C60 molecules, Nat. Commun. 9 (2018) 4177, https://doi.org/10.1038/s41467-018-06437-1.

[66] M. Ashrafizadeh, M. Delfi, A. Zarrabi, A. Bigham, E. Sharifi, N. Rabiee, A.C. Paiva-Santos, A.P. Kumar, S.C. Tan, K. Hushmandi, J. Ren, E.N. Zare, P. Makvandi, Stimuli-responsive liposomal nanoformulations in cancer therapy: pre-clinical & clinical approaches, J. Control. Release 351 (2022), https://doi.org/10.1016/j.jconrel.2022.08.001, 50–80.

[67] M. Ansari, A. Bigham, S.A. Hassanzadeh Tabrizi, H. Abbastabar Ahangar, Copper-substituted spinel Zn-Mg ferrite nanoparticles as potential heating agents for hyperthermia, J. Am. Ceram. Soc. 101 (2018) 3649–3661, https://doi.org/10.1111/jace.15510.

[68] J. Pijuan, C. Barceló, D.F. Moreno, O. Maiques, P. Sisó, R.M. Marti, A. Macià, A. Panosa, In vitro cell migration, invasion, and adhesion assays: from cell imaging to data analysis, Front. Cell Dev. Biol. 7 (2019). https://www.frontiersin.org/articles/10.3389/fcell.2019.00107.

[69] A. Bigham, M.G. Raucci, Multi-responsive materials: properties, design, and applications, ACS Symp. Ser. (2023) 251–273, https://doi.org/10.1021/BK-2023-1436.CH011.

[70] A.D. Dey, A. Bigham, Y. Esmaeili, M. Ashrafizadeh, F.D. Moghaddam, S.C. Tan, S. Yousefiasl, S. Sharma, A. Maleki, N. Rabiee, A.P. Kumar, V.K. Thakur, G. Orive, E. Sharifi, A. Kumar, P. Makvandi, Dendrimers as nanoscale vectors: unlocking the bars of cancer therapy, Semin. Cancer Biol. (2022), https://doi.org/10.1016/J.SEMCANCER.2022.06.003.

[71] I. Fasolino, A. Soriente, M. Caporali, M. Serrano-Ruiz, M. Peruzzini, L. Ambrosio, M.G. Raucci, 2D exfoliated black phosphorus influences healthy and cancer prostate cell behaviors, Sci. Rep. 111 (2021) 1–13, https://doi.org/10.1038/s41598-021-85310-6, 11 (2021).

[72] M. Ashrafizadeh, A. Zarrabi, A. Bigham, A. Taheriazam, Y. Saghari, S. Mirzaei, M. Hashemi, K. Hushmandi, H. Karimi-Maleh, E. Nazarzadeh Zare, E. Sharifi, Y. N. Ertas, N. Rabiee, G. Sethi, M. Shen, Nano)platforms in breast cancer therapy: drug/gene delivery, advanced nanocarriers and immunotherapy, Med. Res. Rev. n/a (2023), https://doi.org/10.1002/med.21971.

[73] Ş. Comşa, A.M. Cîmpean, M. Raica, The story of MCF-7 breast cancer cell line: 40 years of experience in research, Anticancer Res. 35 (2015) 3147. LP – 3154, http://ar.iiarjournals.org/content/35/6/3147.abstract.

[74] C. Pautke, M. Schieker, T. Tischer, A. Kolk, P. Neth, W. Mutschler, S. Milz, Characterization of osteosarcoma cell lines MG-63, saos-2 and U-2 OS in comparison to human osteoblasts, Anticancer Res. 24 (2004) 3743. LP – 3748, http://ar.iiarjournals.org/content/24/6/3743.abstract.

[75] S.C. Moser, B.C.J. van der Eerden, Osteocalcin—a versatile bone-derived hormone, Front. Endocrinol. 9 (2019). https://www.frontiersin.org/articles/10.3389/fendo.2018.00794.

[76] B.R. Barrioni, E. Norris, S. Li, P. Naruphontjirakul, J.R. Jones, M. de M. Pereira, Osteogenic potential of sol–gel bioactive glasses containing manganese, J. Mater. Sci. Mater. Med. 30 (2019) 86, https://doi.org/10.1007/s10856-019-6288-9.

[77] Y. Miao, Y. Chen, J. Luo, X. Liu, Q. Yang, X. Shi, Y. Wang, Black phosphorus nanosheets-enabled DNA hydrogel integrating 3D-printed scaffold for promoting vascularized bone regeneration, Bioact. Mater. 21 (2023) 97–109, https://doi.org/10.1016/J.BIOACTMAT.2022.08.005.

[78] L. Li, X. Liu, B. Gaihre, Y. Li, L. Lu, Mesenchymal stem cell spheroids incorporated with collagen and black phosphorus promote osteogenesis of biodegradable hydrogels, Mater. Sci. Eng. C. 121 (2021) 111812, https://doi.org/10.1016/J.MSEC.2020.111812.

[79] G. Qu, T. Xia, W. Zhou, X. Zhang, H. Zhang, L. Hu, J. Shi, X.F. Yu, G. Jiang, Property-activity relationship of black phosphorus at the nano-bio interface: from molecules to organisms, Chem. Rev. 120 (2020) 2288–2346, https://doi.org/10.1021/ACS.CHEMREV.9B00445/ASSET/IMAGES/LARGE/CR9B00445_0042.JPEG.

[80] G. Brusatin, T. Panciera, A. Gandin, A. Citron, S. Piccolo, Biomaterials and engineered microenvironments to control YAP/TAZ-dependent cell behaviour, Nat. Mater. 17 (2018) 1063–1075, https://doi.org/10.1038/s41563-018-0180-8.